iScience

CellPress
OPEN ACCESS

Article

Microgravity-induced stress mechanisms in human stem cell-derived cardiomyocytes

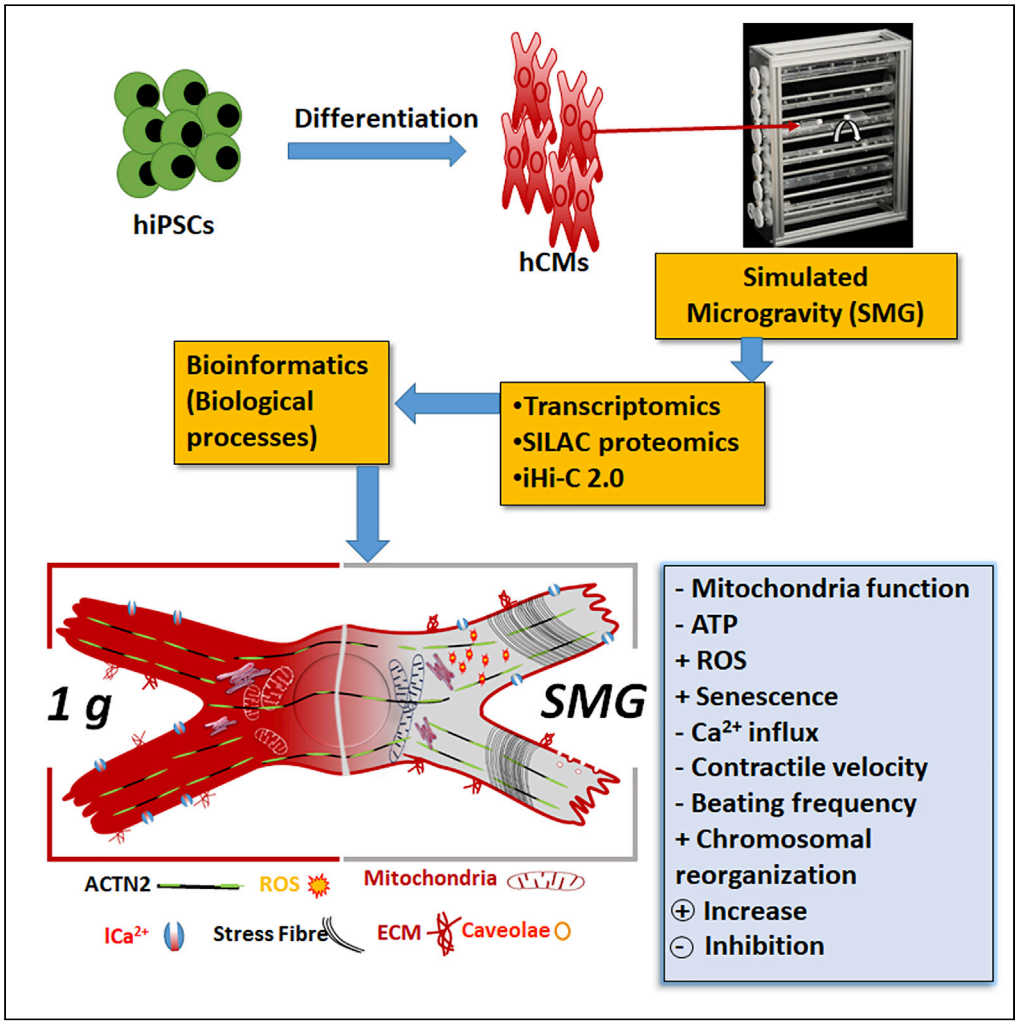

Aviseka Acharya, Harshal Nemade, Symeon Papadopoulos, ..., Athanasia Mizi, Argyris Papantonis, Agapios Sachinidis

a.sachinidis@uni-koeln.de

Highlights

Simulated microgravity (SMG) causes ROS production in human cardiomyocytes (CMs)

SMG inhibits mitochondria function and energy metabolism and induces senescence of CMs

SMG attenuates contractile velocity, beating frequency and Ca^{2+} influx in CMs

SMG induces chromosomal changes and modifies the chromosomal architecture in CMs

Acharya et al., iScience 25, 104577
July 15, 2022
https://doi.org/10.1016/j.isci.2022.104577

iScience

CellPress
OPEN ACCESS

Article

Microgravity-induced stress mechanisms in human stem cell-derived cardiomyocytes

Aviseka Acharya,[1] Harshal Nemade,[1] Symeon Papadopoulos,[1] Jürgen Hescheler,[1] Felix Neumaier,[1] Toni Schneider,[1] Krishna Rajendra Prasad,[1] Khadija Khan,[1] Ruth Hemmersbach,[2] Eduardo Gade Gusmao,[3] Athanasia Mizi,[3] Argyris Papantonis,[3,4,5] and Agapios Sachinidis[1,4,5,6,*]

SUMMARY

Exposure to outer space microgravity poses a risk for the development of various pathologies including cardiovascular disease. To study this, we derived cardiomyocytes (CMs) from human-induced pluripotent stem cells and exposed them to simulated microgravity (SMG). We combined different "omics" and chromosome conformation capture technologies with live-cell imaging of various transgenic lines to discover that SMG impacts on the contractile velocity and function of CMs via the induction of senescence processes. This is linked to SMG-induced changes of reactive oxygen species (ROS) generation and energy metabolism by mitochondria. Taken together, we uncover a microgravity-controlled axis causing contractile dysfunctions to CMs. Our findings can contribute to the design of preventive and therapeutic strategies against senescence-associated disease.

INTRODUCTION

Gravity on Earth has had a documented impact on the development of organisms and is essential for sustaining human life (Demontis et al., 2017; Morey-Holton, 2003). However, life outside the Earth has always intrigued the human mind. Recently, the deep space exploration of Mars have significantly enhanced research on the influence of microgravity on the human body. Over the last 50 years, gravitational biology-related investigations have revealed significant effects of microgravity on organ development using animal models (Ruden et al., 2018). Currently, international space agencies and private corporations are planning missions to the Moon and Mars that require the long presence of humans in space (for a review see ref. (Hughson et al., 2018)).

Studies on astronauts who had remained in space for prolonged periods of time revealed two main risk factors for developing various diseases, including cardiovascular diseases: microgravity and space radiation. In particular, such studies proved that drastic reduction below Earth gravity levels (1 *g*) leads to significant health problems to humans due to their adaptation to outer space microgravity environments (Hughson et al., 2018; Patel, 2020), acting as a major stress stimulus for astronauts. In this context, astronauts are exposed to microgravity for several weeks face such challenges to their health as loss of muscle and bone mass (Demontis et al., 2017; Pelligra et al., 2020), impaired immune defense (Akiyama et al., 2020; Crucian et al., 2018), hematic, metabolic and endocrine complications (Demontis et al., 2017; Pelligra et al., 2020), brain and behavioral complications (Hupfeld et al., 2021), as well as cardiovascular problems (Hughson et al., 2018; Patel, 2020). It therefore becomes obvious that microgravity-related complications are reminiscent of cellular aging processes, in particular of cellular senescence due to reactive oxygen species production (Demontis et al., 2017; Strollo et al., 2018; Vernikos and Schneider, 2010).

Space medicine research, specifically in respect to cardiovascular studies, is of fundamental importance for developing health care interventions for humans with a prolonged exposure to microgravity (Afshinnekoo et al., 2020). To this end, understanding microgravity-induced health complications is a precondition for developing successful therapeutic strategies for humans. Several methodologies have been established for performing *in vivo* (Pandiarajan and Hargens, 2020; Watenpaugh, 2016) and *in vitro* investigations (Kiss et al., 2019) on Earth under artificial microgravity conditions. Such microgravity investigations can be performed using traditional real and simulated microgravity platforms such as drop towers, parabolic flights, sounding rockets and clinostats (Amselem, 2019). However, except for the clinostat platform that allows exposure of cell systems for longer times (up to several days), all other methods induce microgravity acutely for a few seconds to minutes.

[1]University of Cologne, Faculty of Medicine and University Hospital Cologne, Center for Physiology, Working Group Sachinidis, 50931 Cologne, Germany

[2]German Aerospace Center, Institute of Aerospace Medicine, Gravitational Biology, Linder Hoehe, 51147 Cologne, Germany

[3]Institute of Pathology, University Medical Center Göttingen, 37077 Göttingen, Germany

[4]Center for Molecular Medicine Cologne (CMMC), University of Cologne, 50931 Cologne, Germany

[5]These authors contributed equally

[6]Lead contact

*Correspondence: a.sachinidis@uni-koeln.de

https://doi.org/10.1016/j.isci.2022.104577

Due to ethical concerns (Sachinidis et al., 2019), an additional obstacle in ascertaining microgravity mechanisms that are of relevance for humans has been the availability and access to "normal" human cellular systems. Nowadays, human-induced pluripotent stem cell (hiPSC)-derived somatic cells alleviate this obstacle and offer an unlimited source of functional cells, including synchronously beating cardiomyocytes, possessing the key functional properties of cardiomyocytes isolated from human hearts.

To date, because of several experimental limitations, in particular the very short microgravity time exposure of 20 s, deeper insights into the molecular mechanisms induced by microgravity and promoting heart diseases were not possible (Acharya et al., 2019). Here, we address this shortcoming by describing the molecular mechanisms and key features of microgravity-induced senescence in human iPSC-derived cardiomyocytes (CMs) by a combination of high-throughput and functional studies, made possible by their controlled exposure to simulated long-term microgravity (SMG) under 1 *g* laboratory conditions.

RESULTS

Gene expression changes in CMs exposed to SMG at the transcriptome and proteome levels

Purified CMs isolated from hiPSC were exposed to SMG for 48 h (hereafter referred to as "SMG-CMs"). SMG was induced using a slide-flask 2D clinostat device (see STAR Methods for details, Figure S1). Control cardiomyocytes are hereafter referred to as "c-CMs". To assess potential changes in gene expression in CMs exposed to SMG for 48 h, we isolated total cell RNA from SMG- and c-CMs and subjected it to high-throughput sequencing RNA sequencing (RNA-seq). Following data analysis, 825 genes were statistically differentially expressed (DEGs) due to SMG exposure. Of these, ~68% (n = 562) were significantly upregulated and 263 downregulated (Table S1). A query of gene ontology (GO) terms and KEGG/Reactome pathways related to these DEGs via Metascape (Zhou et al., 2019) suggested that SMG promotes adhesion of CMs by upregulating extracellular matrix (ECM) genes (top terms listed in Table 1; complete GO term lists for up- and downregulated genes are shown in Tables S2 and S3, respectively). Moreover, SMG induced hypoxia as cardiomyocytes-expressed genes countering the drop of intracellular oxygen levels. Accordingly, SMG-CMs increased their glycolytic metabolism (as evidenced by induced pyruvate metabolic processes), as well as their contractile activity via genes involved in Ca^{2+} homeostasis. On the other hand, the 263 significantly downregulated genes in SMG-CMs could be linked to reduced ATP production via the inhibition of oxidative phosphorylation. Together, these data suggest that SMG exposure for just 48 h suffices for inducing cellular stress to CMs, primarily reflected in changes to the transcriptome that pertain to mitochondrial structure and functions.

Next, we applied quantitative SILAC-based mass spectrometry to SMG- and c-CMs to capture proteins differentially expressed by SMG. We identified 56 down- and 123 upregulated proteins upon 48 h of microgravity exposure (listed in Table S4). Metascape analysis of GO terms/pathways linked to SMG-upregulated proteins showed that DNA packaging (mostly via histone level changes), chromatin organization, and epigenetic modifiers are strongly affected (Table 2). Notably, SMG also promoted protein expression relevant for oxidative stress-induced senescence, in line with the mito-centric transcriptional changes recorded by RNA-seg (above), as well as changes to ECM components. Proteins downregulated as a result of SMG exposure could be linked to the control of CM growth and to mitophagy (complete GO term lists for up-/downregulated proteins are shown in Tables S5 and S6, respectively). Thus, this proteome-wide analysis also highlights SMG-induced stress to CMs.

Spatial chromosome reorganization follows CM exposure to SMG

Combined, the transcriptome and proteome changes we recorded hinted toward changes in chromosomal conformation. We therefore investigated 3D chromatin architecture changes in SMG-CMs and c-CMs using chromosome conformation capture technology under native conditions (iHi-C). To this end, and given the limited availability of CMs in our SMG experimental set up, we opted for our modified iHi-C 2.0 approach (Mizi et al., 2020) that omits cell fixation, but also incorporates the "easy Hi-C" workflow tailored to low input samples (Lu et al., 2020). Following a novel way for Hi-C data analysis (see STAR Methods for details) and the comparison of the SMG- and c-CM iHi-C matrices, we could identify changes across all levels of 3D genome organization.

First, looking into the organization of the transcriptionally active A- and mostly inactive B-compartments, we found that ~12% switched from A to B, and 6% from B to A. However, these multi-Mbp domains only hosted few of the DEGs recorded above (Figure 1A). Second, we investigated Mbp-sized topologically associating domains (TADs), commonly viewed as the "building blocks of chromosomes" (Beagan and Phillips-Cremins, 2020). Here, >35% of TADs in c-CMs are remodeled in SMG-CMs, with the majority (~25%)

Table 1. Metascape analysis of the upregulated and downregulated genes in SMG-CMs versus the c-CMs; representative BPs, KEGG pathways, and Reactome Gene Sets

Upregulated: Representative enriched BPs and pathways stimulated by SMG				
Term	Description	LogP	Log(q-value)	InTerm_InList
	GO Biological Processes			
GO:0030198	extracellular matrix organization	−32,4	−28,6	54/395
GO:0070482	response to oxygen levels	26,0	−22,4	47/385
GO:0001666	response to hypoxia	−24,0	−20,6	43/348
GO:0036293	response to decreased oxygen levels	−23,4	−20,0	43/360
GO:2000147	positive regulation of cell motility	−15,6	−12,8	43/579
GO:0006090	pyruvate metabolic process	−15,0	−12,2	23/153
GO:0007507	heart development	−14,7	−12,0	41/556
GO:0006096	glycolytic process	−14,4	−11,7	20/114
GO:0031589	cell-substrate adhesion	−13,8	−11,2	32/360
GO:0061718	glucose catabolic process to pyruvate	−12,6	−10,1	11/27
GO:0007160	cell-matrix adhesion	−7,9	−5,8	19/231
GO:0006874	cellular calcium ion homeostasis	−6,9	−4,9	25/443
GO:0055074	calcium ion homeostasis	−6,7	−4,7	25/455
GO:0060047	heart contraction	−6,6	−4,7	19/277
	KEGG Pathway			
ko04512	ECM-receptor interaction	−18,7	−15,6	21/82
ko04510	Focal adhesion	−17,3	−14,4	28/199
ko04151	PI3K-Akt signaling pathway	−12,1	−9,6	29/342
hsa04066	HIF-1 signaling pathway	−11,9	−9,5	18/119
ko00010	Glycolysis/Gluconeogenesis	−10,2	−7,9	13/67
	Reactome Gene Sets			
R-HSA-1474244	Extracellular matrix organization	−33,1	−29,1	49/301
R-HSA-1474290	'Collagen formation	−24,5	−21,0	26/90
R-HSA-216083	Integrin cell surface interactions	−19,7	−16,5	22/85
R-HSA-3000178	ECM proteoglycans	−19,5	−16,3	21/76
R-HSA-1474228	Degradation of the extracellular matrix	−18,1	−15,0	25/140
R-HSA-8948216	Collagen chain trimerization	−17,2	−14,3	16/44
Downregulated (representative enriched BPs and pathways suppressed by SMG)				
	GO Biological Processes			
GO:0006119	oxidative phosphorylation	−33,9	−30,0	32/148
GO:0046034	ATP metabolic process	−26,7	−23,6	35/313
GO:0042773	ATP synthesis coupled electron transport	−26,7	−23,5	24/100
GO:0042775	mitochondrial ATP synthesis coupled electron transport	−26,8	−23,6	24/99
GO:0007005	mitochondrion organization	−15,0	−12,5	31/551
GO:0006123	mitochondrial electron transport, cytochrome c to oxygen	−12,9	−10,6	9/21
GO:0019646	aerobic electron transport chain	−12,9	−10,6	9/21
GO:1902600	proton transmembrane transport	−12,9	−10,5	17/157
GO:0006120	mitochondrial electron transport, NADH to ubiquinone	−10,1	−7,8	10/55
GO:0010257	NADH dehydrogenase complex assembly	−9,4	−7,1	10/65
GO:0042407	cristae formation	−6,1	−4,0	6/35
	KEGG Pathway			
hsa00190	Oxidative phosphorylation	−29,2	−25,9	30/167

(*Continued on next page*)

Table 1. *Continued*

Upregulated: Representative enriched BPs and pathways stimulated by SMG

Term	Description	LogP	Log(q-value)	InTerm_InList
hsa03010	Ribosome	−21,3	−18,5	24/163
hsa04260	Cardiac muscle contraction	−15,6	−13,1	16/91
hsa_M00154	Cytochrome c oxidase	−12,3	−10,0	9/24
	Reactome Gene Sets			
R-HSA-163200	Respiratory electron transport, ATP synthesis by chemiosmotic coupling, and heat production by uncoupling proteins.	−33,3	−29,5	30/125
R-HSA-1428517	The citric acid (TCA) cycle and respiratory electron transport	−28,5	−25,2	30/176
R-HSA-2262752	Cellular responses to stress	−21,4	−18,6	39/584
R-HSA-3700989	Transcriptional Regulation by TP53	−16,0	−13,5	27/365
R-HSA-5628897	TP53 Regulates Metabolic Genes	−14,5	−12,1	15/87
R-HSA-69278	Cell Cycle, Mitotic	−11,5	−9,2	27/561
R-HSA-8949613	Cristae formation	−6,4	−4,3	6/31

splitting into smaller TADs, with ~16% merged into larger TADs (Figure 1B). Third, by plotting the decay of the interaction frequency of chromatin fragments as a function of genomic distance, we observed that longer-range interactions (>20 Mbp in separation) are strengthened upon SMG exposure, potentially indicative of widespread chromosome compaction. At the same time, more proximal interactions are markedly weakened in response to SMG (Figures 1C and 1D). Finally, in an attempt to link 3D chromatin reorganization with SMG-driven gene expression changes, we plotted mean iHi-C signal changes in the 1 Mbp around up-/downregulated gene TSSs. For upregulated TSSs, we observed the focal gain of encompassing interactions, potentially indicative of inclusion in novel sub-Mbp (i.e., TAD-sized) domains (Figure 1E, left panel). For downregulated TSSs, there was a marked gain in shorter (<250-kbp) contacts, again potentially indicative of local chromatin compaction (Figure 1E, right panel).

SMG impacts on the sarcomeric and cytoskeletal structure alignment in CMs

The transcriptome and SILAC-proteome data suggested that SMG modifies CM contractility as well as modify their ECM. Based on these observations, we investigated the effects of SMG on sarcomere assembly by immunostaining for cardiac α-Actinin, as well as by transmission electron microscopy (TEM). Although no significant changes in the morphology of SMG-CM sarcomeres were observed (Figure 2A), TEM revealed the formation of stress fibers and membrane caveolae in a subset of SMG-CMs (Figure 2B). Such fibers and caveolae are characteristic changes to the cell membrane due to mechanical stress (Echarri and Del Pozo, 2015). The formation of caveolae in SMG-CMs could be also confirmed by Western blotting showing higher levels of CAV1 as compared to c-CMs (Figure 2C). These findings suggest that although SMG exposure does not lead to significant sarcomere disassembly, it does induce stress fiber and caveolae in SMG-CMs.

Effects of SMG on mitochondrial structure, function, and ATP synthesis

Given the physiology of CMs, focused on executing synchronous beating, the formation of caveolae and stress fibers is possibly indicative of effects on contractility. To assess this, we further evaluated different aspects of mitochondrial function under SMG (as also hinted by our Metascape analyses; see Tables 1 and 2). First, in order to monitor ROS in the mitochondria, we generated DyRed1-E5$^+$-CMs after differentiation of DyRed1-E5$^+$-hiPSCs and exposed them to SMG for 48 h. DyRed1-E5 is a mutant form of the DsRed protein that is mitochondrial-targeted and sensitive to free radicals (Figure S2). It changes its fluorescence from green to red in response to increased ROS levels and/or to high mitochondrial turnover. In positive control experiments, DyRed1-E5$^+$ c-CMs were treated with H_2O_2, which increases intracellular ROS. This resulted in almost complete elimination of green fluorescent signal from the cells (Figure 3B). Similarly, high-resolution image analysis of DyRed1-E5$^+$ SMG-CMs also revealed mitochondria with intense red fluorescence indicative of accumulating of ROS in response to SMG (see representative Video S1), which was not the case for DyRed1-E5$^+$ c-CMs (see representative Video S2 and Figure 3B).

Table 2. Metascape analysis of the SILAC-upregulated and downregulated proteins in SMG-CMs versus the c-CMs; Representative BPs, KEGG pathways, and Reactome Gene Sets

Term	Description	LogP	Log(q-value)	InTerm_InList
Upregulated: Representative enriched BPs and pathways stimulated by SMG)				
	GO Biological Processes			
GO:0071103	DNA conformation change	−26,1	−22,8	26/323
GO:0071824	protein-DNA complex subunit organization	−23,1	−20,3	23/282
GO:0006342	chromatin silencing	−22,2	−19,4	18/133
GO:0065004	protein-DNA complex assembly	−21,7	−19,0	21/242
GO:0006323	DNA packaging	−21,4	−18,8	20/211
GO:0045814	negative regulation of gene expression, epigenetic	−21,4	−18,8	18/146
GO:0006333	chromatin assembly or disassembly	−19,2	−16,7	18/192
GO:0006281	DNA repair	−11,0	−8,6	18/567
GO:0030198	extracellular matrix organization	−9,2	−6,9	14/395
GO:0042254	ribosome biogenesis	−7,4	−5,2	11/307
	KEGG Pathway			
hsa04217	Necroptosis	−18,7	−16,2	17/168
ko03030	DNA replication	−10,0	−7,7	7/36
ko04512	ECM-receptor interaction	−8,9	−6,6	8/82
hsa04510	Focal adhesion	−5,6	−3,5	8/215
ko04151	PI3K-Akt signaling pathway	−4,2	−2,1	8/342
	Reactome Gene Sets			
R-HSA-3214815	HDACs deacetylate histones	−28,8	−25,2	20/94
R-HSA-5334118	DNA methylation	−26,2	−22,9	17/65
R-HSA-212300	PRC2 methylates histones and DNA	−25,3	−22,1	17/73
R-HSA-2559586	DNA Damage/Telomere Stress Induced Senescence	−24,5	−21,4	17/80
R-HSA-4839726	Chromatin organization	−23,4	−20,5	23/274
R-HSA-3214847	HATs acetylate histones	−23,3	−20,4	19/142
R-HSA-212165	Epigenetic regulation of gene expression	−21,2	−18,6	18/149
R-HSA-2559582	Senescence-Associated Secretory Phenotype (SASP)	−20,1	−17,6	16/112
R-HSA-2559580	Oxidative Stress Induced Senescence	−19,3	−16,8	16/125
Downregulated: Representative enriched BPs and pathways suppressed by SMG				
	GO Biological Processes			
GO:0097352	autophagosome maturation	−6,1	−2,6	4/46
GO:0010038	response to metal ion	−5,9	−2,6	7/352
GO:0000422	autophagy of mitochondrion	−5,2	−2,1	4/75
GO:0016049	cell growth	−5,0	−2,0	7/473
GO:0007005	mitochondrion organization	−4,6	−1,8	7/551
GO:1901137	carbohydrate derivative biosynthetic process	−4,5	−1,8	8/783
GO:0040017	positive regulation of locomotion	−4,3	−1,7	7/607
GO:0006695	cholesterol biosynthetic process	−3,7	−1,2	3/73
GO:0042391	regulation of membrane potential	−3,2	−0,9	5/431
	KEGG Pathway			
ko00520	Amino sugar and nucleotide sugar metabolism	−6,0	−2,6	4/48
	Reactome Gene Sets			
R-HSA-1474244	Extracellular matrix organization	−3,9	−1,4	5/301
R-HSA-556833	Metabolism of lipids	−2,2	−0,2	5/740

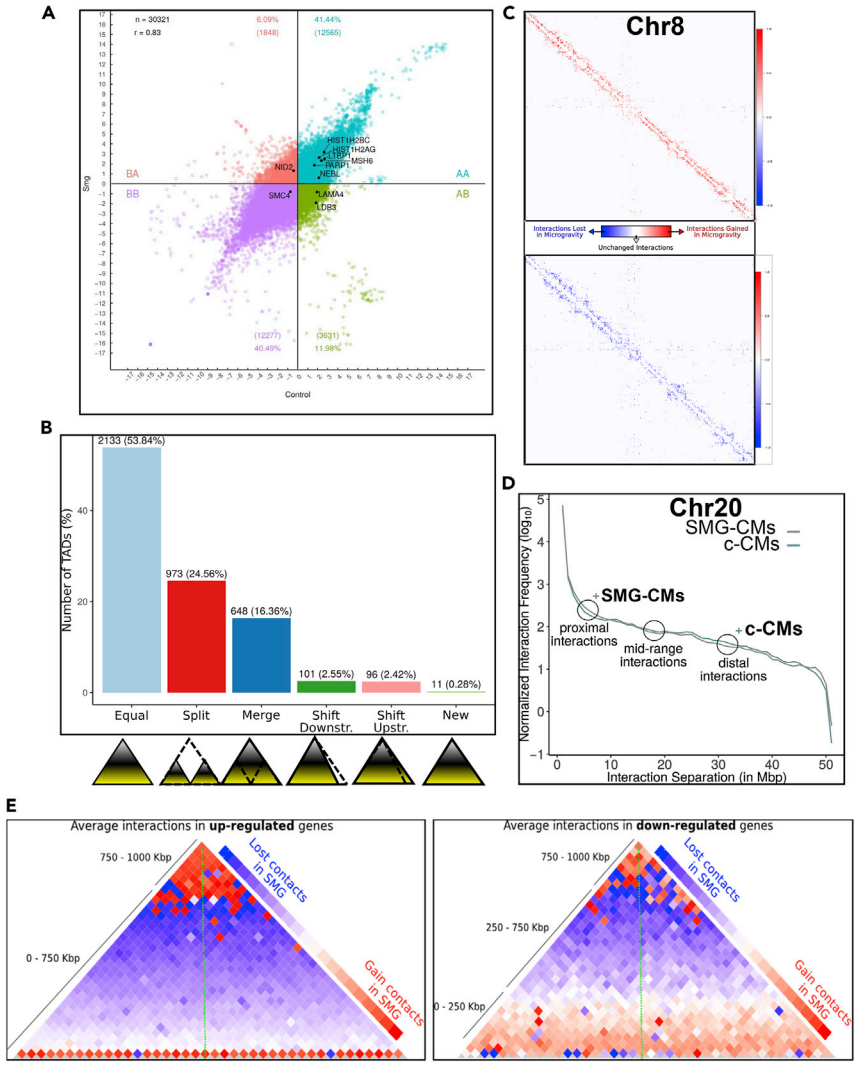

Figure 1. Compartments and topologically associated domains (TADs) in SMG-CMs and in c-CMs and interactions gained in SMG-CMs versus c-CMs

(A) Each point represents 100 Kbp regions that belongs to the A or B compartments for the c-CMs (x axis) and SMG-CMs (y axis). This shows the differential compartments between the different experiments.

(B) In this plot, on the right you can see the proportion of TADs called in 1 *g* that changed or maintained its status in SMG.

(C and D) Interactions gained in SMG-CMs are proximal while interactions lost are distal. C, Chromosome 8 with interactions gained in SMG-CMs (red contact map) and lost in SMG (blue contact map).

(D) Interaction-decay plots for chr20.

(E) Upregulated and downregulated genes in SMG lose both proximal and intermediary interactions. The promoter of the gene is in the center of the maps shown by the dashed green lines. In this averaged differential contact maps, blue colors indicate interactions lost in SMG and red colors indicate interactions gained in SMG.

Next, mitochondrial membrane potential in SMG-CMs versus c-CMs was determined using the JC-1 staining. The JC-1 dye is a lipophilic, cationic dye that enters and accumulates into mitochondria to form so-called "J-aggregates". Monomeric JC-1 emits green fluorescence, whereas J-aggregates present as red in functionally intact negatively charged mitochondria with a normal membrane potential. In contrast, in non-intact (damaged) mitochondria, JC-1 entry is greatly impeded due to loss of mitochondrial membrane potential resulting in a reduction in J-aggregates; then, monomeric JC-1 retains its green signal. As shown in Figure 3A, a decrease of the red fluorescence intensity was observed in SMG-CMs in parallel with increased green signal, suggesting the impairment (or full loss) of mitochondrial membrane potential (Figure 3A). As a consequence of mitochondrial potential dysfunctions, ATP synthesis is expected to be compromised. We

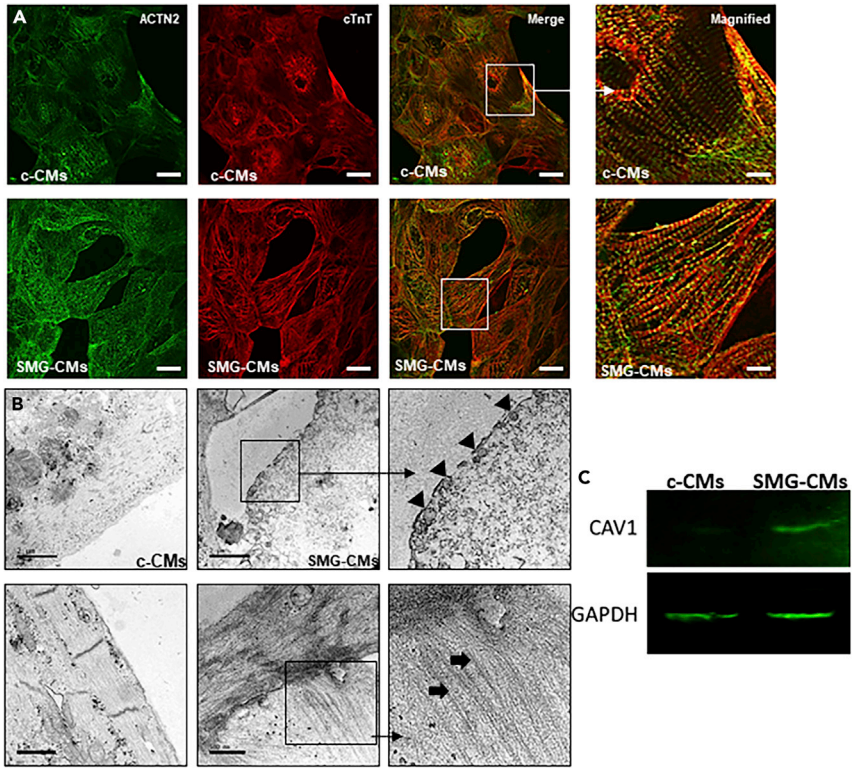

Figure 2. Exposure to SMG does not cause cytoskeletal deteriorations in CMs

(A) A representative immunofluorescence staining of sarcomeric α-actinin (ACTN2) and cardiac troponin T (cTnT) in c-CMs and SMG-CMs (scale bar: 10 μm).

(B) TEM images of SMG-CMs and c-CMs. Black arrow heads indicate caveolae structures (black arrows show stress fibers (scale bar: 500 nm).

(C) Western blot analysis of Caveolin (CAV1) in control and SMG-exposed CMs (molecular weight of 22 kDa). GAPDH (36 kDa) was used as an internal protein loading control.

therefore determined ATP levels in SMG- and c-CMs using a luminescence-based assay. 48 h of SMG exposure resulted in an almost 45% reduction of the ATP synthesis in SMG-CMs compared to controls (Figure 3C).

Finally, our Metascape analyses also identified changes in genes relevant to mitochondrial organization (Tables 1 and 2). We followed this up by investigating mitochondria morphology under SMG using TEM. SMG exposure of CMs led to the hyperfusion of mitochondria, which were also morphologically different compared to those in c-CMs, with SMG-CM mitochondria appearing ~40% longer than control ones (Figure 3D). These findings further support our hypothesis that SMG exposure leads to impaired mitochondrial turnover and therefore promotes a senescence-like phenotype in CMs.

SMG induces an increase of ROS, RNS, and stimulates the β-galactosidase activity in CMs

Our transcriptome analysis showed significant upregulation of genes involved in senescence and oxidative stress pathways in SMG-CMs. To prove whether cellular ROS and RNS production is generally increased in SMG-CMs, we next performed DHE (di-hydro-ethidium) stainings after 48 h of SMG exposure. In the absence of excessive ROS, DHE remains cytosolic and emits blue fluorescence. Upon oxidization by free radicals, DHE is converted into ethidium bromide that enters the nucleus and binds DNA to emit red fluorescence. SMG-CM nuclei present with significantly increased levels of red signal (i.e., ~4-fold more red dots compared to c-CMs; Figure 4A). As shown in Figure 4B, we could confirm the SMG-induced increase of ROS in IMR90- and iCell-CM by applying the fluorescence DCFH-DA ROS assay. These findings confirm the accumulation of substantial ROS amounts following 48 h exposure of CMs to SMG. The reactive nitrogen species (RNS) family of molecules is formed from nitric oxide (NO) generated by the nitric oxide synthase (NOS) and superoxide anion (O_2^-) produced by the NADPH oxidase, respectively. We also assessed RNS production in SMG-CMs, to identify additional reactive species (Figure 4C). Last, to confirm senescence induction in SMG-CMs, cells were cultured in the presence of the

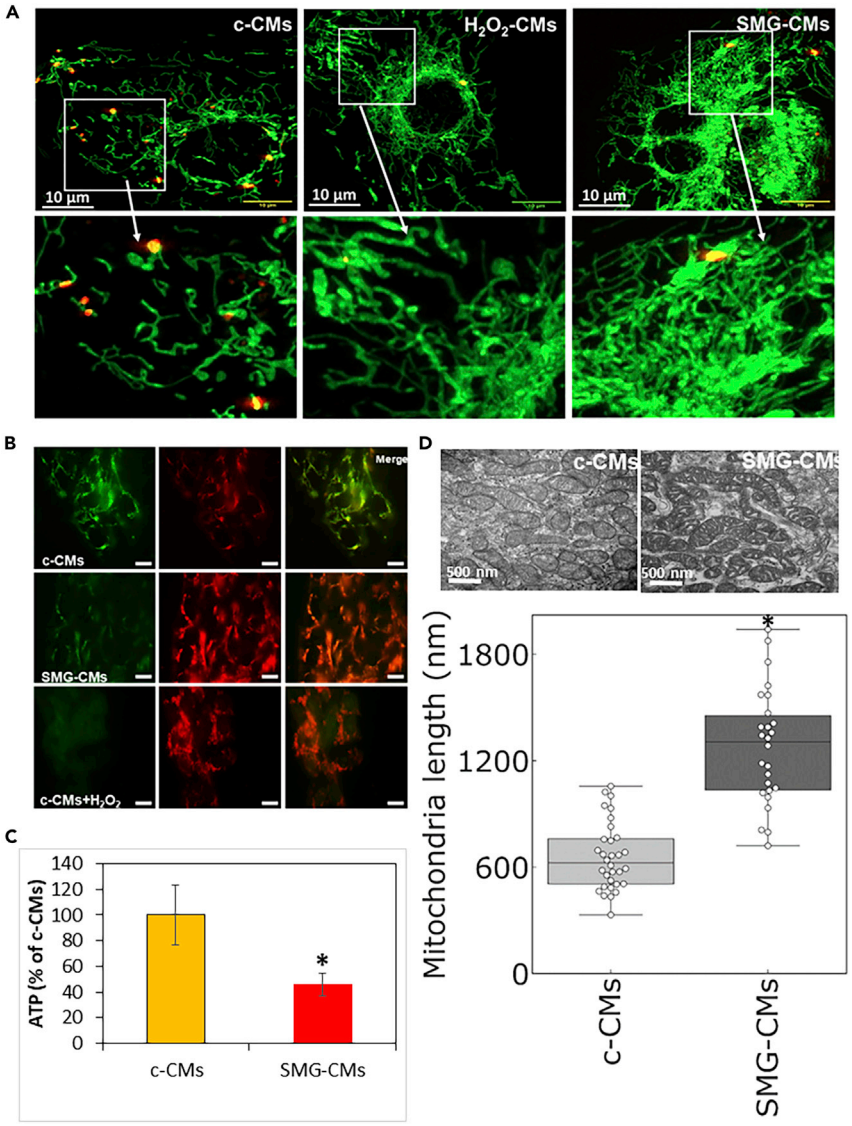

Figure 3. Effects of 48 h SMG on mitochondrial morphology, ROS production, membrane potential, and ATP synthesis

(A) Mitochondria staining of the SMG-CMs and c-CMs with the JC-1 dye to visualize disturbances in mitochondrial membrane potential (MMP). The JC-1 dye is a lipophilic, cationic dye that can be accumulated into the mitochondria to form the J-aggregates. The monomeric JC-1 naturally exhibits green fluorescence, whereas the JC-1 aggregates exhibit red fluorescence. Intact cells exhibit normal mitochondrial membrane potential. In this case, JC-1 dye enters and accumulates more in the negatively charged mitochondria and emits red fluorescent hence mitochondria appear redder as compared to mitochondria emitting green fluorescence. In contrast, JC-1 incorporation into mitochondria is greatly hindered due to the loss of mitochondrial membrane potential resulting in a reduction of J-aggregate formation retaining in its original green fluorescence. Both, monomers (green) and aggregates (red) were captured by using a confocal laser scanning microscope. The images were then processed and analyzed by using the ImageJ software. The ratio of green vs red color represents disturbances of the mitochondrial membrane potential; the greener; the intact mitochondria) (scale bar = 10 µm).

(B) Fluorescence lifetime imaging microscopy (FLIM) of DyRed1-E5^{+}-CMs (see video record 2 and DyRed1-E5^{+}-SMG-CMs (see record 3) (Excitation length 488 nm). Visualization of newly synthesized and non-oxidized MitoTimer was performed setting an emission length of 497–531 nm (green color); Oxidized DyRed1-E5 was visualized at a fluorescence length of 583–695 nm. The ratio of green vs red fluorescence is representative for the overall mitochondrial turnover in the cells (scale bar: 20 µm).

Figure 3. *Continued*

(C) ATP level in SMG-CMs and c-CMS. Total intracellular ATP was quantified using the ATPlite Luminescence ATP Detection Assay System. ATP levels were expressed as a per cent of the c-CMs levels (100%) (mean ± SD; n = 12, *p < 0.05; two-tailed t-test; three independent experiments; each experiment was performed in triplicate wells).

(D) TEM images showing mitochondrial morphology and cristae structures in 48 h SMG-CMs versus control c-CMs (scale bar: 500 nm). The maximum number of mitochondria from 5 images from 3 independent experiments (3 separate slides) was selected. The quantification of the mitochondrial length was performed using the ImageJ software and plotted as a boxplot.

CellEvent™ Senescence Green Probe, a fluorogenic substrate; β-galactosidase processes this substrate inside of the cell to emit a fluorescence signal. 48 h of SMG exposure led to a 3-fold increase in β-gal-positive CMs compared to control titers (Figures 4D and 4E).

SMG disrupts calcium flux in CMs

Our "omics" data pointed to several genes involved in calcium homeostasis and ion transport being deregulated in SMG-CMs, including *G6PD*, *P2RX4*, *TSPO*, *ASPH*, *DMD*, *CACNA1C*, *NOL3*, *END1*, *CAV1*, *APP*, *CACR4*, *STC1*, *KCNA5*, *SLC38A1*, *RYR2*, and *ATP1A2*. Therefore, we extended our studies to monitor Ca^{2+} flux in SMG—as compared to c-CMs. Cells were loaded with FLUO4-AM to monitor sarcoplasmic Ca^{2+} concentration ($[Ca^{2+}]_i$) transients during CM contraction. Transients were analyzed for the following kinetic parameters: time-to-peak (TTP, the time between the start and the peak (F_{max}) of the transient), $(\Delta F/\Delta T)_{max}$ (the maximal slope within the TTP period), and T90% (the time for 90% decay from F_{max}). Exposure to SMG for 48 h had a significant impact on the kinetics of calcium transients in CMs, while no differences in sarcoplasmic resting $[Ca^{2+}]$ were observed (Figure 5A). We did observe a significant reduction in (ΔF/ΔT)max in SMG-CMs, indicating a slower rise in sarcoplasmic $[Ca^{2+}]$(Figure 5B). Accordingly, TTP displayed a significant increase (Figure 5C). Removal of Ca^{2+} from sarcoplasm was also slower in SMG-CMs, as indicated by the significantly longer T90% interval (Figure 5D). To monitor potential differences in the electrophysiology of Ca^{2+} currents between SMG-CMs and c-CMs, patch-clamp experiments were performed. Ca^{2+} currents were elicited by depolarization from the holding potential to potentials ranging from −60 to +60 mV and were normalized to the membrane capacitance (pA/pF, current density). As illustrated in Figure 5E, the pA/pF ratios in SMG-CMs were significantly lower than those recorded in c-CMs, indicative of significantly lower net sarcolemmal Ca^{2+} entry following SMG exposure (Figure 5E). This finding indicates that SMG could impair normal L-type calcium channel (LTCC) function. Since RYR2 and phospholamban are critical elements for the kinetics of sarcoplasmic Ca^{2+} release and its reuptake into the sarcoplasmic reticulum, we tested whether the expression of the two proteins is affected in SMG-CMs. Western blot analysis revealed a reduction of the levels of both proteins (Figure 5F).

SMG affects the contraction and relaxation velocity of beating CMs

To investigate the effects of SMG on the contraction and relaxation velocity of CM sarcomeres, we generated one more transgenic iPSC line, ACTN2-eGFP$^+$-hiPSCs (Figure S3), allowing the generation of ACTN2-eGFP$^+$-CMs and real-time monitoring of several parameters characteristic of CM functionality. ACTN2 is a cardiac-specific cytoskeletal protein localizing to the Z-discs and playing a vital role in cardiac contractions. Using this line, we can identify ACTN2-rich Z-discs based on fluorescence in both control and SMG-CMs (Figures 6A and 6B). Figures 6C and 6D show representative measurements of the contraction and relaxation velocities recorded in c-CMs and SMG-CMs, respectively (data extracted from Videos S3 and S4, respectively, using the MATLAB-based SRAC-TRAC tool (Toepfer et al., 2019)). These recordings allowed detailed monitoring and analysis of contraction and relaxation of the individual z-discs. After analysis of the data generated from 6 independant experiments, we observed significant reduction in both contraction and relaxation velocities in SMC-CMs compared to c-CMs (Figures 6E and 6F). In addition, we also observed longer TTP duration in SMG-CMs while the contraction velocity sloped (Figure 6G), and the beating rate was significantly reduced (Figures 6H and 6I). In general, cardiomyocytes were responded to the adrenoreceptor agonist Isoprenaline (Video S5), and to the L-type agonist Bay-K8864 (Video S6) (see STAR Methods).

DISCUSSION

Human heart remodeling has been extensively studied under microgravity conditions and it is characterized by reduced oxygen metabolism and atrophy (Patel and Kos, 2005; Perhonen et al., 2001; Summers et al., 2005). Understanding the molecular mechanisms behind these phenotypes is of fundamental importance for developing preventive and therapeutic strategies against disease stemming from such environmental factors such as microgravity and radiation. To this end, we used IMR90-hiPSCs-derived CMs to identify here a microgravity-controlled axis causing a senescence-like phenotype leading to

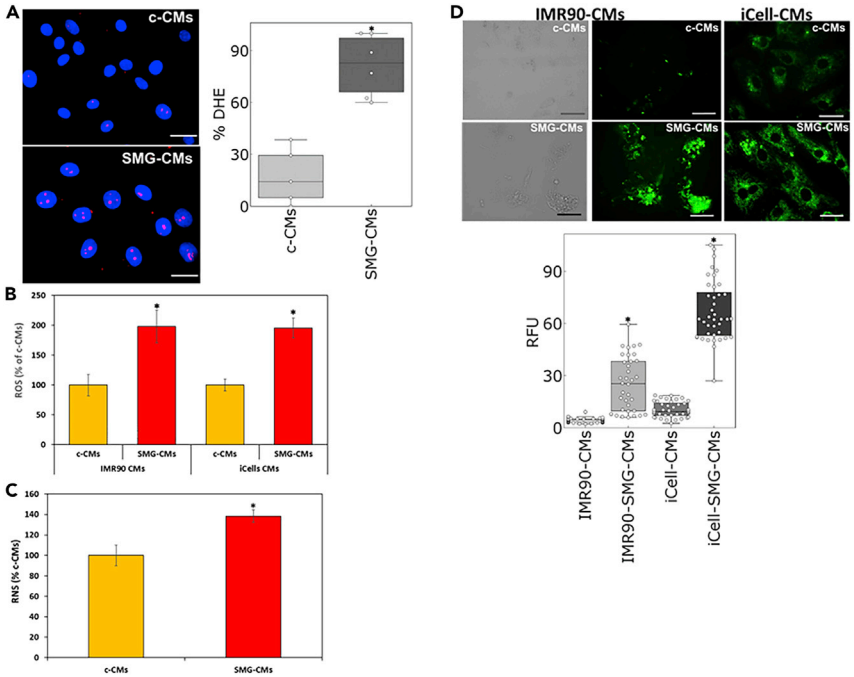

Figure 4. Effects of SMG on ROS, RNS production, and β-galactosidase activity in CMs

(A) Fluorescent images showing an increase in DHE staining in SMG-CMs in comparison to c-CMs. Red staining in nuclei indicates a net increase in the ROS production (Nuclei: DAPI) (Scale bar: 20 μm). Quantification was performed using ImageJ software (red: nuclear DHE; blue: DAPI). Five images of c-CMs (in total n = 71 cells) and SMG-CMs (in total n = 53 cells) from tree independent experiments (3 slides) were selected and all the cells in each image were counted for positive and negative red nuclear staining. Then, the percent positive staining was calculated and represented in the graph as % DHE staining (Mean ± SD, $p < 0.05$).

(B) ROS quantification in c-CMs and SMG-CMs by the fluorescence DCFH-DA test. The fluorescence intensity was measured using Softmax Pro M5e 96-well plate reader with excitation and emission wavelengths of 485 and 535 nm, respectively. All the fluorescence intensities are normalized with control c-CMs (100%) (Mean ± SD, $p < 0.05$, n = 9, three independent experiments, performed in triplicates).

(C) Reactive nitrogen species (RNS) production in SMG-CMs and c-CMs. Fluorescence was quantified in a fluorometric plate reader at 480 nm/530 nm (expressed as percent of the absolute values of RNS in c-CMs (mean ± SD, $p < 0.05$, n = 9, two-tailed t-test; three independent experiments, performed in triplicates).

(D) Bright filter and fluorescent images showing increase β-galactosidase staining in SMG-CMs and c-CMs (Scale bar = 50 μM) in IMR90-and iCell-CMs. Quantification of the GFP intensity from 35 CMs from each condition (c-CMs and SMG-CMs, 3 independent experiments) was determined by the ImageJ software. Then, the raw intensity data were plotted as a box plot.

contractile dysfunctions in CMs. To get evidence that SMG may induce also atrophy of the CMs, we investigated the effects of SMG on the expression of three genes *MurF1*, *FOXO* and *SMAD3* that serve as markers for cardiomyocytes atrophy (Du et al., 2021; Ni et al., 2006; Tsui et al., 2015; Xin et al., 2017). As indicated in Figure S4 the, expression of all three genes was significantly upregulated in comparison to c-CMs.

Cellular senescence is one of the causal processes of aging. It invokes molecular cascades countering cell death when cells are exposed to various stress conditions. In the senescent state, cells are metabolically active, but no longer replicating (Payea et al., 2021). Senescence is also implicated in the development of aging-related disease (van Deursen, 2014). The main hallmarks for CM senescence are DNA damage response (DRS), mitochondria dysfunction, compromised contractile behavior, as well as hypertrophy (Tang et al., 2020). Our "omics" data analysis of genes and proteins differentially expressed following microgravity exposure suggested that SMG triggers mitochondrial-dependent senescence and modifies mitochondrial turnover (i.e., the adaptation of mitochondrial volume, content, and activity to current cellular energy needs) in CMs. This can be attributed to elevated oxidative stress levels, as ROS production can drive CMs to a senescent state, explain the imbalance between energy demand and supply (Ruiz-Meana et al., 2019), and lead to full-fledged heart disease (Kuster et al., 2010; Tian et al., 2021).

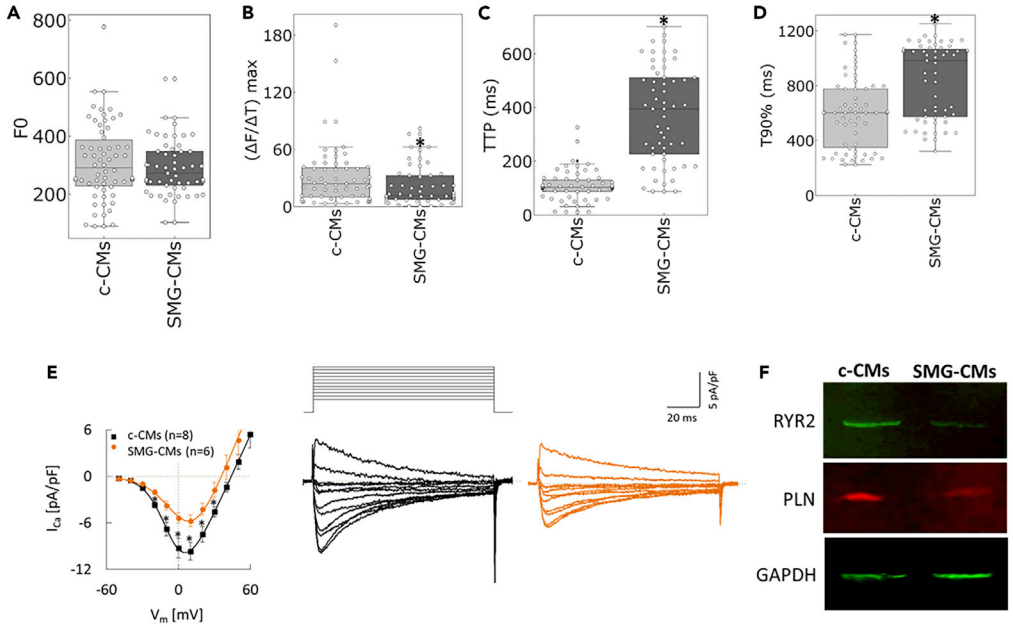

Figure 5. Effects of SMG on Ca^{2+} handling of CMs

(A–D) SMG-CMs and c-CMs were loaded with FLUO4-AM and line scans were performed using a FV1000 Olympus microscope with a 60× oil immersion objective and the 488 nm argon line for excitation. After capturing the [Ca^{2+}] transients, background correction was applied before performing the line scan data analysis using Sigma Plot (Version 8.04, SPSS) and a self-made Excel macro. The calculated [Ca^{2+}] transient parameters were (A) the relative amplitude (F/F0 where F0 is the resting fluorescence intensity in arbitrary units), (B) the time-to-peak (TTP), (C) the maximum slope of the rise in ΔF ($[\Delta F/\Delta T]_{max}$) and (D) the time for the transient to decay to 10% of the F/F0 peak (T90%). For both SMG and c-CMs, we recorded seventy independent readings to perform a robust statistical analysis. Values in A–D represent the mean ± SD (*$p < 0.05$, $n = 70 \pm 5$; two-tailed t-test). E, Voltage-gated calcium currents in SMG-CMs (orange) and c-CMs (black). Current densities (pA/pF) were determined by the patch-clamp technique in the whole-cell configuration. Barium was used as a charge carrier (Mean ± SD, $n = 8$ for c-CMs and $n = 6$ for SMG-CMs, *$p < 0.05$; two-tailed t-test. F, effect of SMG-CMs on the expression of RYR2 and phospholamban protein.

ROS is available in at least eight cellular compartments, namely in mitochondria, lysosomes, endoplasmic reticulum, the Golgi, peroxisomes, the nucleus, and in the cytosol (Naviaux, 2012; Zorov et al., 2014). Cytosolic ROS could trigger complex cellular signaling pathways that induce ROS release from mitochondria, a process known as the ROS-induced ROS release mechanism (RIRR) (for review see (Zorov et al., 2014)). Indeed, we demonstrated that SMG caused a significant increase in cellular ROS. However, further studies are required to demonstrate whether the RIRR mechanism is involved in the SMG-induced increase of the ROS level. As indicated in Figure S4, the expression of the antioxidant genes, superoxide dismutase 2, mitochondrial (SOD2), and catalase (CAT) was upregulated in the SMG-CMs. The upregulation of the antioxidant enzyme SOD2 may occur due to a potential inactivation of the SMG-induced increase of intracellular ROS thereby preventing the senescent CMs from cell death. However, this hypothesis should be underpinned by extensive enzymatic and other assays.

We also examined the effect of the SMG on the cell viability of the IMR90 CMs and iCell CMs. As shown in Figure S5, the cell viability of the CMs which were exposed to 48 h SMG was approximately 85%, whereas further decreased by 74% after 72 h SMG. Therefore, we suggest that a 48 h SMG duration time is an optimal period for our SMG-related investigations. Our viability data suggest that during 48 h SMG most of the cells are in the senescent stage avoiding an extensive cell death that can happen extensively due to a syndrome of stress signals, e. g., due to starvation of the cells. Moreover, during the 48 h SMG period, no exchange of the medium is required. A SMG period of more than 48 h would necessitate medium exchange under 1 *g* conditions and therefore would lead to inconsistent findings. Interestingly, we identified by our Metascape analysis that 27 genes belonging to the p53 pathway and 8 genes belonging to TOR pathway whose expression was suppressed in SMG-CMs (see Table S3 and Table S7A). Normally, these pathways are involved in cell death processes but senescent cells, in general, are resistant to apoptosis and cell death (for review see (Hu et al., 2022). Therefore, we may speculate

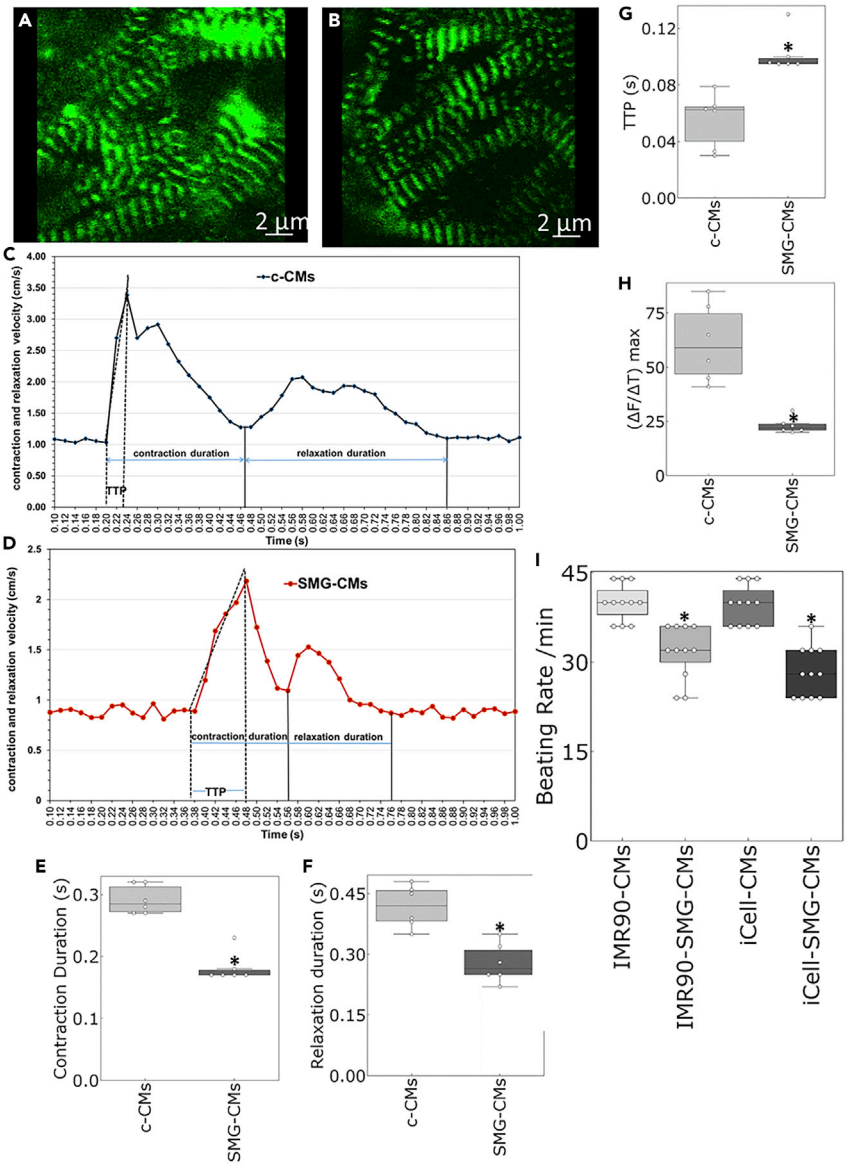

Figure 6. Live imaging of contraction and relaxation velocity activity of ACTN2-eGPF^{+}-CMs and ACTN2-eGPF^{+}-SMG-CMs

(A and B) Fluorescence microscopy shows the Z-discs of ACTN2-eGPF^{+}-CMs in c-CMs and ACTN2-eGPF^{+}-SMG-CMs (ACTN2 is enriched in Z-discs) immediately after 48 h SMG. ACTN2 Video record 4 and 5 shows the contractile activity of the c-CMs and SMG-CMs, respectively. Fluorescence microscopy has been performed using the Olympus FluoView1000 confocal system C–D, Contractile velocity of c-CMs and SMG-CMs (representative experiments; see Videos S3 and S4, respectively) was determined by analyzing the video records 4 and 5 (50fps), respectively by using the VA1.9 software. E–G, Diagrams show the duration of contraction, the duration of relaxation, and the TTP values and of the c-CMs and SMG-CMs, respectively (mean ± SD, n = 6,*p < 0.05; two-tailed t-test; 3 independent experiments). H, Diagram shows the $\Delta V/\Delta T)_{max}$ ratio in SMG-CMs versus c-CMs ((mean ± SD, n = 6,*p < 0.05; two-tailed t-test; 6 independent experiments). I, beating frequency of SMG-CMs *versus* c-CMs (mean ± SD, n = 11,*p < 0.05; 3; two-tailed t-test; independent experiments).

that the SMG-CMs suppressed genes associated with these pathways preventing senescent CMs from apoptosis and cell death.

In our study system, this is evident in the effects SMG has on the contractile function of CMs. By challenging intracellular Ca^{2+} homeostasis, SMG led to rhythmic changes in the contraction and relaxation times of CMs. The increase in contraction velocity slopes recorded in SMG-CMs is indicative of SMG acting as

negative inotropic factor. This likely manifests as a result of cell membrane destabilization, as evidenced by the structural deformities and caveolae formation observed in SMG-CMs. In addition, the higher T_{90} values in SMG-CMs suggest a delayed Ca^{2+} removal from the sarcoplasm of these cells. Such a change in intracellular Ca^{2+} clearance rates has also been observed in aged mice cardiomyocytes (Yang et al., 2006) and may be justified by an impaired function of SERCA2a. We have demonstrated that the Ca^{2+} influx was significantly lower in SMG-CMs (Figure 5E). On the other hand, the expression of several calcium ion homeostasis genes (Table S2 and Table S7B) was upregulated although cardiac muscle contraction-specific genes were significantly downregulated (Table S3 and Table S7C). From these findings, we may speculate that the L-type calcium channel (LTCC) activity is impaired in SMG-CMs via biomechanical mechanisms.

Finally, the onset of senescence has been shown to confer dramatic changes to 3D genome organization, including reshuffling of TADs (Zirkel et al., 2018) and chromatin compaction (Criscione et al., 2016). Given that gene expression changes induced by SMG resembled those seen in replicative senescence, we used iHi-C and could show that similar changes occur in CMs under SMG conditions. On the one hand, we recorded strengthened longer-range interactions at the expense of shorter-range ones, which can be indicative of chromatin compaction. But, in contrast to what occurs during replicative senescence, we find that the majority of TADs that change their boundaries due to SMG appear to split into smaller domains ((in senescence the major effect is TAD merging; (Zirkel et al., 2018)). This difference could well be due to the post-mitotic nature of CMs or a signature of SMG-induced genome reorganization.

More recently, human Jurkat T cells were exposed to short-term gravitational changes in parabolic flight and suborbital ballistic rocket flight experiments (Vahlensieck et al., 2021). Authors reported that smaller chromosomes (Chr 16–22 except for chr18) have higher intrachromosomal interactions compared to large chromosomes in altered gravity. However, it should be pointed out, that during the parabolic flight, the Jurkat T cells were exposed to 31 alternating hypergravity, microgravity, and hypergravity phases, each lasting 20–22 sec (Acharya et al., 2019). In striking contrast, in the present study, CMs were continuously exposed exclusively to microgravity for 48 h. Therefore, due to fundamental experimental differences of the Hi-C data in our study and the study reported (Vahlensieck et al., 2021) are not surprising. Nevertheless, it is evident that SMG also impacts large-scale chromosomal organization.

However, to validate our key findings, we also repeated some key experiments with the commercially available iCell-CMs. The iCell-CMs were derived from hiPSCs after reprogramming blood cells (according to the declarations of the Cellular Dynamics). Again, SMG induced an elevation of intracellular ROS level, an increase of the β-galactosidase activity and significantly reduced the beating frequency of the iCell-CMs. Also, similar effects of SMG were observed regarding the viability of the IMR90-CMs and iCell-CMs. However, the comparative experiments were performed with purified cardiomyocytes in the absence of other non-myocyte cells such as cardiac fibroblasts which may affect the function of cardiomyocytes. This limitation can be improved by investigating the effects of SMG on 3D cardiac organoids consisting of cardiomyocytes and non-myocyte cells such as fibroblasts and endothelial cells.

Overall, our observations are consistent with the impairment of CM contractile function owing to challenges in mitochondrial metabolism, which is a fundamental aspect of cardiac aging (Barton et al., 2017). Taken together, despite some limitations, our results can lay the foundation for developing strategies to prevent senescence processes in the heart and to develop new therapeutics against microgravity-induced disease.

Limitations of the study

There are three limitations of the present study. One important limitation is the use of the hiPSC-derived cardiomyocytes which till now are not mature although they are fully functional. The other limitation is the short time of 48 h exposure under simulated microgravity conditions. Indeed, experiments under real microgravity conditions onaboard the International Space Station (ISS) for a longer period would be optimal. Finally, further experiments are needed to demonstrate whether the senescence processes are reversible in the presence and absence of anti-senescence compounds.

STAR★METHODS

Detailed methods are provided in the online version of this paper and include the following:

- KEY RESOURCES TABLE

SUPPLEMENTAL INFORMATION

Supplemental information can be found online at https://doi.org/10.1016/j.isci.2022.104577.

ACKNOWLEDGMENT

This work was supported by the Bundesministerium für Wirtschaft und Energie (BASIS2: 50WB1929; awarded to A.S.) and by the Deutsche Forschungsgemeinschaft via a Basic Module grant and the SPP2202 Priority Program (Project Nr. 285697699 and 422389065, respectively; both awarded to A.P.).

AUTHOR CONTRIBUTIONS

A.A. conducted the main experiments, collected all the findings, and contributed to the writing of the manuscript. K.P. and K.K. contributed to the experimental part. H.N. generated the plasmids for the study. S.P. conducted the Ca^{2+} measurements. F.N., J.H., and T.S. conducted and supervised the patch-clamp experiments. R.H. supervised the simulated microgravity experiments. A.M. conducted iHi-C experiments and E.G.G. the bioinformatic analysis of the iHi-C data. A.P. contributed to the analysis and interpretation of data, and to the writing of the manuscript. A.S. designed and supervised the study, interpreted data, conducted analysis of "omics" data, and wrote the manuscript.

DECLARATION OF INTERESTS

The authors declare no competing interests.

Received: October 27, 2021
Revised: March 25, 2022
Accepted: June 7, 2022
Published: July 15, 2022

REFERENCES

Acharya, A., Brungs, S., Lichterfeld, Y., Hescheler, J., Hemmersbach, R., Boeuf, H., and Sachinidis, A. (2019). Parabolic, flight-induced, acute hypergravity and microgravity effects on the beating rate of human cardiomyocytes. Cells *8*, 352. https://doi.org/10.3390/cells8040352.

Acharya, A., Nemade, H., Rajendra Prasad, K., Khan, K., Hescheler, J., Blackburn, N., Hemmersbach, R., Papadopoulos, S., and Sachinidis, A. (2022). Live-cell imaging of the contractile velocity and transient intracellular Ca(2+) fluctuations in human stem cell-derived cardiomyocytes. Cells *11*, 1280. https://doi.org/10.3390/cells11081280.

Afshinnekoo, E., Scott, R.T., MacKay, M.J., Pariset, E., Cekanaviciute, E., Barker, R., Gilroy, S., Hassane, D., Smith, S.M., Zwart, S.R., et al. (2020). Fundamental biological features of spaceflight: advancing the field to enable deep-space exploration. Cell *183*, 1162–1184. https://doi.org/10.1016/j.cell.2020.10.050.

Akiyama, T., Horie, K., Hinoi, E., Hiraiwa, M., Kato, A., Maekawa, Y., Takahashi, A., and Furukawa, S. (2020). How does spaceflight affect the acquired immune system? NPJ Microgravity *6*, 14. https://doi.org/10.1038/s41526-020-0104-1.

Amselem, S. (2019). Remote controlled autonomous microgravity lab platforms for drug research in space. Pharmaceut. Res. *36*, 183. https://doi.org/10.1007/s11095-019-2703-7.

Barton, G.P., de Lange, W.J., Ralphe, J.C., Aiken, J., and Diffee, G. (2017). Linking metabolic and contractile dysfunction in aged cardiac myocytes. Physiological Rep. *5*, e13485. https://doi.org/10.14814/phy2.13485.

Beagan, J.A., and Phillips-Cremins, J.E. (2020). On the existence and functionality of topologically associating domains. Nat. Genet. *52*, 8–16. https://doi.org/10.1038/s41588-019-0561-1.

Chen, X., Wei, S., Ji, Y., Guo, X., and Yang, F. (2015). Quantitative proteomics using SILAC: principles, applications, and developments. Proteomics *15*, 3175–3192. https://doi.org/10.1002/pmic.201500108.

Correia, C., Koshkin, A., Duarte, P., Hu, D., Teixeira, A., Domian, I., Serra, M., and Alves, P.M. (2017). Distinct carbon sources affect structural and functional maturation of cardiomyocytes derived from human pluripotent stem cells. Sci. Rep. *7*, 8590.

Criscione, S.W., Teo, Y.V., and Neretti, N. (2016). The chromatin landscape of cellular senescence. Trends Genet. *32*, 751–761. https://doi.org/10.1016/j.tig.2016.09.005.

Crowe, A.R., and Yue, W. (2019). Semi-quantitative determination of protein expression using immunohistochemistry staining and analysis. An integrated protocol. Bio. Protoc. *9*, e3465.

Crucian, B.E., Choukèr, A., Simpson, R.J., Mehta, S., Marshall, G., Smith, S.M., Zwart, S.R., Heer, M., Ponomarev, S., Whitmire, A., et al. (2018). Immune system dysregulation during spaceflight: potential countermeasures for deep space exploration missions. Front. Immunol. *9*, 1437. https://doi.org/10.3389/fimmu.2018.01437.

Demontis, G.C., Germani, M.M., Caiani, E.G., Barravecchia, I., Passino, C., and Angeloni, D. (2017). Human pathophysiological adaptations to the space environment. Front. Physiol. *8*, 547. https://doi.org/10.3389/fphys.2017.00547.

Du, F., Cao, Y., Ran, Y., Wu, Q., and Chen, B. (2021). Metformin attenuates angiotensin II-induced cardiomyocyte hypertrophy by upregulating the MuRF1 and MAFbx pathway. Exp. Ther. Med. *22*, 1231. https://doi.org/10.3892/etm.2021.10665.

Durand, N.C., Shamim, M.S., Machol, I., Rao, S.S., Huntley, M.H., Lander, E.S., and Aiden, E.L. (2016). Juicer provides a one-click system for analyzing loop-resolution Hi-C experiments. Cell Syst *3*, 95–98. https://doi.org/10.1016/j.cels.2016.07.002.

Echarri, A., and Del Pozo, M.A. (2015). Caveolae – mechanosensitive membrane invaginations linked to actin filaments. J. Cell Sci. *128*, 2747–2758. https://doi.org/10.1242/jcs.153940.

Eiermann, P., Kopp, S., Hauslage, J., Hemmersbach, R., Gerzer, R., and Ivanova, K. (2013). Adaptation of a 2-D clinostat for simulated microgravity experiments with adherent cells. Microgravity Sci. Technol. *25*, 153–159. https://doi.org/10.1007/s12217-013-9341-1.

Gusmao, E.G., Mizi, A., Brant, L., and Papantonis, A. (2020). Retrieving high-resolution chromatin interactions and decoding enhancer regulatory potential *in silico*. Preprint at bioRxiv. https://doi.org/10.1101/2020.11.10.376533.

Hamill, O.P., Marty, A., Neher, E., Sakmann, B., and Sigworth, F.J. (1981). Improved patch-clamp techniques for high-resolution current recording from cells and cell-free membrane patches. Pflügers Archiv *391*, 85–100. https://doi.org/10.1007/bf00656997.

Hernandez, G., Thornton, C., Stotland, A., Lui, D., Sin, J., Ramil, J., Magee, N., Andres, A., Quarato, G., Carreira, R.S., et al. (2013). MitoTimer: a novel tool for monitoring mitochondrial turnover. Autophagy *9*, 1852–1861. https://doi.org/10.4161/auto.26501.

Hu, L., Li, H., Zi, M., Li, W., Liu, J., Yang, Y., Zhou, D., Kong, Q.-P., Zhang, Y., and He, Y. (2022). Why senescent cells are resistant to apoptosis: an insight for senolytic development. Front. Cell Dev. Biol. *10*, 822816. https://doi.org/10.3389/fcell.2022.822816.

Huang, K., Chen, W., Zhu, F., Li, P.W.-L., Kapahi, P., and Bai, H. (2019). RiboTag translatomic profiling of Drosophila oenocytes under aging and induced oxidative stress. BMC Genom. *20*, 50. https://doi.org/10.1186/s12864-018-5404-4.

Hughson, R.L., Helm, A., and Durante, M. (2018). Heart in space: effect of the extraterrestrial environment on the cardiovascular system. Nat. Rev. Cardiol. *15*, 167–180. https://doi.org/10.1038/nrcardio.2017.157.

Hupfeld, K.E., McGregor, H.R., Reuter-Lorenz, P.A., and Seidler, R.D. (2021). Microgravity effects on the human brain and behavior: dysfunction and adaptive plasticity. Neurosci. Biobehav. Rev. *122*, 176–189. https://doi.org/10.1016/j.neubiorev.2020.11.017.

Kiss, J.Z., Wolverton, C., Wyatt, S.E., Hasenstein, K.H., and van Loon, J.J.W.A. (2019). Comparison of microgravity analogs to spaceflight in studies of plant growth and development. Front. Plant Sci. *10*, 1577. https://doi.org/10.3389/fpls.2019.01577.

Knight, P.A., and Ruiz, D. (2012). A fast algorithm for matrix balancing. IMA J. Numer. Anal. *33*, 1029–1047. https://doi.org/10.1093/imanum/drs019.

Kruse, K., Hug, C.B., Hernández-Rodríguez, B., and Vaquerizas, J.M. (2016). TADtool: visual parameter identification for TAD-calling algorithms. Bioinformatics *32*, 3190–3192. https://doi.org/10.1093/bioinformatics/btw368.

Kuster, G.M., Häuselmann, S.P., Rosc-Schlüter, B.I., Lorenz, V., and Pfister, O. (2010). Reactive oxygen/nitrogen species and the myocardial cell homeostasis: an ambiguous relationship. Antioxidants Redox Signal. *13*, 1899–1910. https://doi.org/10.1089/ars.2010.3464.

Laker, R.C., Xu, P., Ryall, K.A., Sujkowski, A., Kenwood, B.M., Chain, K.H., Zhang, M., Royal, M.A., Hoehn, K.L., Driscoll, M., et al. (2014). A novel MitoTimer reporter gene for mitochondrial content, structure, stress, and damage in vivo. J. Biol. Chem. *289*, 12005–12015. https://doi.org/10.1074/jbc.m113.530527.

Lian, X., Hsiao, C., Wilson, G., Zhu, K., Hazeltine, L.B., Azarin, S.M., Raval, K.K., Zhang, J., Kamp, T.J., and Palecek, S.P. (2012). Robust cardiomyocyte differentiation from human pluripotent stem cells via temporal modulation of canonical Wnt signaling. Proc. Natl. Acad. Sci. USA *109*, E1848–E1857. https://doi.org/10.1073/pnas.1200250109.

Lu, L., Liu, X., Huang, W.K., Giusti-Rodríguez, P., Cui, J., Zhang, S., Xu, W., Wen, Z., Ma, S., Rosen, J.D., et al. (2020). Robust Hi-C maps of enhancer-promoter interactions reveal the function of non-coding genome in neural development and diseases. Mol. Cell *79*, 521–534.e15. https://doi.org/10.1016/j.molcel.2020.06.007.

Mellacheruvu, D., Wright, Z., Couzens, A.L., Lambert, J.P., St-Denis, N.A., Li, T., Miteva, Y.V., Hauri, S., Sardiu, M.E., Low, T.Y., et al. (2013). The CRAPome: a contaminant repository for affinity purification-mass spectrometry data. Nat. Methods *10*, 730–736. https://doi.org/10.1038/nmeth.2557.

Mizi, A., Gade Gusmao, E., and Papantonis, A. (2020). iHi-C 2.0: a simple approach for mapping native spatial chromatin organisation from low cell numbers. Methods *170*, 33–37. https://doi.org/10.1016/j.ymeth.2019.07.003.

Morey-Holton, E.R. (2003). 9 - the impact of gravity on life. In Evolution on Planet Earth, L.J. Rothschild and A.M. Lister, eds. (Academic Press), pp. 143–159.

Naviaux, R.K. (2012). Oxidative shielding or oxidative stress? J. Pharmacol. Exp. Therapeut. *342*, 608–618. https://doi.org/10.1124/jpet.112.192120.

Nemade, H., Acharya, A., Chaudhari, U., Nembo, E., Nguemo, F., Riet, N., Abken, H., Hescheler, J., Papadopoulos, S., and Sachinidis, A. (2020). Cyclooxygenases inhibitors efficiently induce cardiomyogenesis in human pluripotent stem cells. Cells *9*, 554.

Nemade, H., Chaudhari, U., Acharya, A., Hescheler, J., Hengstler, J.G., Papadopoulos, S., and Sachinidis, A. (2018). Cell death mechanisms of the anti-cancer drug etoposide on human cardiomyocytes isolated from pluripotent stem cells. Arch. Toxicol. *92*, 1507–1524. https://doi.org/10.1007/s00204-018-2170-7.

Ni, Y.G., Berenji, K., Wang, N., Oh, M., Sachan, N., Dey, A., Cheng, J., Lu, G., Morris, D.J., Castrillon, D.H., et al. (2006). Foxo transcription factors blunt cardiac hypertrophy by inhibiting calcineurin signaling. Circulation *114*, 1159–1168. https://doi.org/10.1161/circulationaha.106.637124.

Novo, E., and Parola, M. (2008). Redox mechanisms in hepatic chronic wound healing and fibrogenesis. Fibrogenesis Tissue Repair *1*, 5. https://doi.org/10.1186/1755-1536-1-5.

O'Brien, J., Hayder, H., and Peng, C. (2016). Automated quantification and analysis of cell counting procedures using ImageJ plugins. J Vis *Exp*,, 54719.

Pandiarajan, M., and Hargens, A.R. (2020). Ground-based analogs for human spaceflight. Front. Physiol. *11*, 716. https://doi.org/10.3389/fphys.2020.00716.

Patel, R., and Kos, L. (2005). Endothelin-1 and neuregulin-1 convert embryonic cardiomyocytes into cells of the conduction system in the mouse. Dev. Dynam. *233*, 20–28. https://doi.org/10.1002/dvdy.20284.

Patel, S. (2020). The effects of microgravity and space radiation on cardiovascular health: from low-Earth orbit and beyond. Int J Cardiol Heart Vasc *30*, 100595. https://doi.org/10.1016/j.ijcha.2020.100595.

Payea, M.J., Anerillas, C., Tharakan, R., and Gorospe, M. (2021). Translational control during cellular senescence. Mol. Cell Biol. *41*. https://doi.org/10.1128/mcb.00512-20.

Pelligra, S., Casstevens, E.A., Matthews, M.J., and Edemekong, P.F. (2020). Aerospace health maintenance wellness. In StatPearls (Treasure Island (FL) (StatPearls Publishing). Copyright © 2020, StatPearls Publishing LLC.

Perhonen, M.A., Franco, F., Lane, L.D., Buckey, J.C., Blomqvist, C.G., Zerwekh, J.E., Peshock, R.M., Weatherall, P.T., and Levine, B.D. (2001). Cardiac atrophy after bed rest and spaceflight. J. Appl. Physiol. *91*, 645–653. https://doi.org/10.1152/jappl.2001.91.2.645.

Rao, S.S.P., Huang, S.C., Glenn St Hilaire, B., Engreitz, J.M., Perez, E.M., Kieffer-Kwon, K.R., Sanborn, A.L., Johnstone, S.E., Bascom, G.D., Bochkov, I.D., et al. (2017). Cohesin loss eliminates all loop domains. Cell *171*, 305–320.e24. https://doi.org/10.1016/j.cell.2017.09.026.

Ruden, D.M., Bolnick, A., Awonuga, A., Abdulhasan, M., Perez, G., Puscheck, E.E., and Rappolee, D.A. (2018). Effects of gravity, microgravity or microgravity simulation on early mammalian development. Stem Cell. Dev. *27*, 1230–1236. https://doi.org/10.1089/scd.2018.0024.

Ruiz-Meana, M., Minguet, M., Bou-Teen, D., Miro-Casas, E., Castans, C., Castellano, J., Bonzon-Kulichenko, E., Igual, A., Rodriguez-Lecoq, R., Vázquez, J., and Garcia-Dorado, D. (2019). Ryanodine receptor glycation favors mitochondrial damage in the senescent heart. Circulation *139*, 949–964. https://doi.org/10.1161/circulationaha.118.035869.

Sachinidis, A. (2021). High-throughput base editing: a promising technology for precision medicine and drug discovery. Signal Transduct. Targeted Ther. *6*, 221. https://doi.org/10.1038/s41392-021-00633-0.

Sachinidis, A., Albrecht, W., Nell, P., Cherianidou, A., Hewitt, N.J., Edlund, K., and Hengstler, J.G. (2019). Road map for development of stem cell-based alternative test methods. Trends Mol. Med. *25*, 470–481. https://doi.org/10.1016/j.molmed.2019.04.003.

Strollo, F., Gentile, S., Strollo, G., Mambro, A., and Vernikos, J. (2018). Recent progress in space physiology and aging. Front. Physiol. *9*, 1551. https://doi.org/10.3389/fphys.2018.01551.

Summers, R.L., Martin, D.S., Meck, J.V., and Coleman, T.G. (2005). Mechanism of spaceflight-induced changes in left ventricular mass. Am. J. Cardiol. *95*, 1128–1130. https://doi.org/10.1016/j.amjcard.2005.01.033.

Tang, X., Li, P.-H., and Chen, H.-Z. (2020). Cardiomyocyte senescence and cellular communications within myocardial microenvironments. Front. Endocrinol. *11*, 280. https://doi.org/10.3389/fendo.2020.00280.

Tian, R., Xu, J., Luo, Q., Hou, C., and Liu, J. (2021). Rational design and biological application of antioxidant nanozymes. Front. Chem. *8*, 831. https://doi.org/10.3389/fchem.2020.00831.

Toepfer, C.N., Sharma, A., Cicconet, M., Garfinkel, A.C., Mücke, M., Neyazi, M., Willcox, J.A.L., Agarwal, R., Schmid, M., Rao, J., et al. (2019). SarcTrack. Circ. Res. *124*, 1172–1183. https://doi.org/10.1161/circresaha.118.314505.

Tohyama, S., Hattori, F., Sano, M., Hishiki, T., Nagahata, Y., Matsuura, T., Hashimoto, H., Suzuki, T., Yamashita, H., Satoh, Y., et al. (2013). Distinct metabolic flow enables large-scale purification of mouse and human pluripotent stem cell-derived cardiomyocytes. Cell Stem Cell *12*, 127–137. https://doi.org/10.1016/j.stem.2012.09.013.

Tsui, H., Zi, M., Wang, S., Chowdhury, S.K., Prehar, S., Liang, Q., Cartwright, E.J., Lei, M., Liu, W., and Wang, X. (2015). Smad3 couples Pak1 with the antihypertrophic pathway through the E3 ubiquitin ligase, Fbxo32. Hypertension *66*, 1176–1183. https://doi.org/10.1161/hypertensionaha.115.06068.

Tyanova, S., Temu, T., and Cox, J. (2016). The MaxQuant computational platform for mass spectrometry-based shotgun proteomics. Nat. Protoc. *11*, 2301–2319. https://doi.org/10.1038/nprot.2016.136.

Vahlensieck, C., Thiel, C.S., Zhang, Y., Huge, A., and Ullrich, O. (2021). Gravitational force-induced 3D chromosomal conformational changes are associated with rapid transcriptional response in human T cells. Int. J. Mol. Sci. *22*, 9426. https://doi.org/10.3390/ijms22179426.

van Deursen, J.M. (2014). The role of senescent cells in ageing. Nature *509*, 439–446. https://doi.org/10.1038/nature13193.

Vernikos, J., and Schneider, V.S. (2010). Space, gravity and the physiology of aging: parallel or convergent disciplines? A mini-review. Gerontology *56*, 157–166. https://doi.org/10.1159/000252852.

Walter, A., Šarić, T., Hescheler, J., and Papadopoulos, S. (2016). Calcium imaging in pluripotent stem cell-derived cardiac myocytes. Methods Mol. Biol. *1353*, 131–146. https://doi.org/10.1007/7651_2015_267.

Watenpaugh, D.E. (2016). Analogs of microgravity: head-down tilt and water immersion. J. Appl. Physiol. *120*, 904–914. https://doi.org/10.1152/japplphysiol.00986.2015.

Xin, Z., Ma, Z., Jiang, S., Wang, D., Fan, C., Di, S., Hu, W., Li, T., She, J., and Yang, Y. (2017). FOXOs in the impaired heart: new therapeutic targets for cardiac diseases. Biochim. Biophys. Acta (BBA) - Mol. Basis Dis. *1863*, 486–498. https://doi.org/10.1016/j.bbadis.2016.11.023.

Yang, X., Doser, T.A., Fang, C.X., Nunn, J.M., Janardhanan, R., Zhu, M., Sreejayan, N., Quirin, M.T., Ren, J., Yang, X., et al. (2006). Metallothionein prolongs survival and antagonizes senescence-associated cardiomyocyte diastolic dysfunction: role of oxidative stress. FASEB. J. *20*, 1024–1026. https://doi.org/10.1096/fj.05-5288fje.

Zhou, Y., Zhou, B., Pache, L., Chang, M., Khodabakhshi, A.H., Tanaseichuk, O., Benner, C., and Chanda, S.K. (2019). Metascape provides a biologist-oriented resource for the analysis of systems-level datasets. Nat. Commun. *10*, 1523. https://doi.org/10.1038/s41467-019-09234-6.

Zirkel, A., Nikolic, M., Sofiadis, K., Mallm, J.-P., Brackley, C.A., Gothe, H., Drechsel, O., Becker, C., Altmüller, J., Josipovic, N., et al. (2018). HMGB2 loss upon senescence entry disrupts genomic organization and induces CTCF clustering across cell types. Mol. Cell *70*, 730–744.e6. https://doi.org/10.1016/j.molcel.2018.03.030.

Zorov, D.B., Juhaszova, M., and Sollott, S.J. (2014). Mitochondrial reactive oxygen species (ROS) and ROS-induced ROS release. Physiol. Rev. *94*, 909–950. https://doi.org/10.1152/physrev.00026.2013.

STAR★METHODS

KEY RESOURCES TABLE

REAGENT or RESOURCE	SOURCE	IDENTIFIER
Antibodies		
Anti-Caveolin-1	ab18199	Abcam
anti RYR2	ab219798	Abcam
anti GAPDH	ABS16	Sigma
anti PLN	MA3-922	Thermo Fisher Scientific
anti-cardiac Troponin T	MA5-12960	Thermo Fisher Scientific
Bacterial and virus strains		
Stellar Competent Cells	636766	TAKARA Bio
One Shot™ TOP10 Chemically Competent *E. coli*	C404010	Thermo Fisher Scientific
Chemicals, peptides, and recombinant proteins		
Dihydroethidium (DHE), Blue fluorescent dye	ab145360	Abcam
L-Arginine-HCl	89989	Thermo Fisher Scientific
L-Lysine-2HCl	89987	Thermo Fisher Scientific
L-Arginine-HCl, 13C6, 15N4	89990	Thermo Fisher Scientific
L-Lysine-2HCl, 13C6, 15N2	88209	Thermo Fisher Scientific
Critical commercial assays		
Applied Biosystems™ SYBR™ Green PCR Master Mix	43-444-63	Applied Biosystems™
ATPlite Luminescence Assay System	6016943	Perkin Elmer
β-galactosidase staining kit	C10850	Thermo Fisher Scientific
OxiSelect Intracellular ROS Assay Kit (Green Fluorescence)	MBS168048	MyBiosource
MitoProbe™ JC-1 Assay Kit	M34152/22204	Thermo Fisher Scientific
Deposited data		
RNAseq transcriptome data	This paper	ArrayExpress, EMBL-EBI Datasets platform: E-MTAB-11159
iHiC2.0 data	Mizi et al. (2020); Methods 170, 33-37	https://www.ncbi.nlm.nih.gov/geo/query/acc.cgi?acc=GSE161636
Experimental models: Cell lines		
IMR90 hiPSCs	iPS(IMR90)-4-DL-1 p18+34(9)	Wisconsin International Stem Cell Bank
iCell Cardiomyocytes	iCell Cardiomyocytes, 11713	Cellular Dynamics, Fujifilm
Oligonucleotides		
Primers for qRT-PCR for several genes	See Table S8	Integrated DNA Technology (IDT), Integrated DNA Technology, Leuven, Belgium
Recombinant DNA		
pMitoTimer	52659	Addgene
pCAG-PBase	40972	Addgene
PB-TA-ERP2	80477	Addgene
pGP-CMV-GCaMP6s	40753	Addgene
PB-TAC-ERP2	80478	Addgene
cACTN2 tagging	N-Terminal CopGFP tagging	CRISPR/Alstem Bio
IMR90-ACTN2-copGFP		Custom made

(*Continued on next page*)

Continued

REAGENT or RESOURCE	SOURCE	IDENTIFIER
Software and algorithms		
ImageJ for fluorescent image analysis	(Crowe and Yue, 2019; O'Brien et al., 2016)	https://imagej.nih.gov/ij/
Video Analyzer 1.9	GitHub software reposity; Acharya et al. (2022); 11:1280. https://doi.org/10.3390/cells11081280	https://github.com/nblackburn123/Video-Analyser/releases/tag/v1.9
Maxquant (version 1.5.3.8)	Nat Protoc *11*, 2301–2319.	https://www.maxquant.org/
Other		
iHiC2.0	Mizi et al. (2020); Methods 170, 33-37	https://www.sciencedirect.com/science/article/abs/pii/S1046202319300106

RESOURCE AVAILABILITY

Lead contact

Further information and requests for resources and reagents should be directed to and will be fulfilled by the lead contact, Agapios Sachinidis (a.sachinidis@uni-koeln.de).

Materials availability

All reagents will be made available. The following cell lines will be available after completion of a Materials Transfer Agreement.

- A transgenic ACTN2-eGFP^{+}-hiPSCs line (IMR90).
- A transgenic Tet-inducible MitoTimer hiPSCs line (IMR90).
- IMR90-ACTN2-copGFP (recombinant DNA).

Data and code availability

- The RNAseq transcriptome data were deposited on the ArrayExpress EMBL-EBI Datasets platform (accession number: E-MTAB-11159.
- The iHi-C 2.0 data were deposited on NCBI, GEO (accession number GSE16163).
- The paper does not report original codes and reagents. All codes and reagents used in this study are listed in the key resources table".Any additional information required to reanalyze the data reported in this paper is available from the lead contact upon request.

METHOD DETAILS

Differentiation of hiPSC into cardiomyocytes

Experiments were performed with the IMR90 hiPSC (authorized by the Robert-Koch Institute; Berlin, Germany, license number: AZ 3.04.0210083). Cells were cultured on matrigel-coated Petri dishes. Cells were cultured in StemMACS™ iPS-Brew XF media (Milteny Biotech, Germany) supplemented with 50 U/mL penicillin and 50 U/mL streptomycin (Thermo Fisher Scientific, MA, USA), at 37°C and 5% CO_2. After reaching of a confluence of 90%, cells were dissociated by trypsinization using the trypLE solution (Thermo Fisher Scientific, MA, USA) and propagation of the cells was performed in StemMACS™ iPS-Brew XF media in the presence of 10 μM ROCK inhibitor. Differentiation of hiPSCs to cardiomyocytes was performed by a combination of two differentiations protocols (Lian et al., 2012; Tohyama et al., 2013) as we described previously (Nemade et al., 2020). The cells were cultured in RPMI1640/B-27$^{-\text{insulin medium}}$ (Medium without insulin (B-27$^{-\text{insulin medium}}$) in the presence of 10 μM CHIR99021 (Tocris, United Kingdom) for 24 h (day 1). Then the culture medium was replaced with a normal RPMI/B-27$^{+\text{insulin medium}}$ and cells were cultured for further 24 h (day 2). Then the culture medium was replaced with RPMI/B-27$^{-\text{insulin media}}$ containing 10 μM IWP2 (Tocris, United Kingdom) and cells were cultured for a further 48 h (day 4). Then the medium was replaced with basal RPMI/B-27$^{-\text{insulin}}$ medium and was refreshed every 2 days. Spontaneous beating cardiomyocytes were observed from day 8 onwards. Enrichment of the cardiomyocytes was performed by culturing the cells with glycose-free RPMI (Thermo Fisher Scientific, MA, US) containing 4 μM sodium DL-lactate for 6 days. The purity of cardiomyocytes at day 18 of

differentiation % was evaluated by fluorescence-activated cell sorting (FACS) analysis. The FACS analysis was performed as previously described in (Nemade et al., 2020). In brief, the beating CM clusters were dissociated into single cells using StemPro® Accutase® Cell Dissociation Reagent (Thermo Fisher, MA, US) and fixed with ice-cold 90% Methanol for 10 min at room temperature. Post fixing the cells were stained with anti-cTnT antibody (ab209813, Abcam) in DPBS plus 0.1% Triton X-100 and 0.5% BSA followed by goat anti-rabbit IgG (Alexa Fluor® 488, Abcam, ab150077). Flow cytometric data were collected and analyzed using Attune® Acoustic Focusing Cytometer and Attune® Cytometric Software v2.1 (AppliedBiosystems, CA, US) respectively. As shown in Figure S6 the purity was over 90%. The additional characterisation was done by the gene expression of cardiomyocytes specific genes by RT-PCR and by immunostaining of cardiomyocytes specific cytoskeletal proteins. Cardiomyocytes were responded to the adrenoreceptor agonist Isoprenaline (Video S5), to the L-type agonist Bay-K8864 (Video S6), each at a concentration of 1 μM, with an increase of beating activity and the L-Type blocker Nifedipine (1 μM) completely blocked the beating activity of the cardiomyocytes. Then hCMs were trypsinized and seeded it into different plastic materials which were pre-coated with fibronectin. Seeding of the cells was performed in DMEM containing 5% foetal calf serum (FBS). The CMs were cultured in a modified cardiomyocytes maturation medium (Correia et al., 2017) in a 5% CO_2 incubator at 37°C for further 12 days before starting the experiments. The modified maturation medium was composed of glycose-free RPMI supplemented with 4 mM L-lactate (Sigma Aldrich, 71718), 5 mM creatine monohydrate (Sigma Aldrich, C3630), 2 mM taurine (Sigma Aldrich, T0625), 2 mM L-carnitine (Sigma Aldrich, C0283), 0.5 mM ascorbic acid (Sigma Aldrich, A8960), 1× Linoleic Acid-Oleic Acid-Albumin 100× (sigma, L9655-5ML), NEAA (Thermo Fisher Scientific, 11140), 1× B27 media and 1% KOSR (Thermo Fisher Scientific, 10828028).

The commercially available iCell cardiomyocytes were obtained from Cellular Dynamics (iCell-CMs). According to the declarations of the company, the CMs were derived from hiPSCs after reprograming blood cells (according to the declarations of the Cellular Dynamics; https://www.fujifilmcdi.com/products/cardiac-cells/icell-cardiomyocytes). The culturing conditions were similar to for the IMR90 hiPSCs-derived cardiomyocytes.

Slide flask clinostat

The Slide-flask 2D-clinostat device as shown in Figure S1 was custom manufactured in DLR, Cologne, Germany as described previously (Eiermann et al., 2013). This device is used to generate simulated microgravity at samples by rotating around an axis parallel to the force of gravity. It is designed with 6 rotating arms and each arm can hold 4 slide customized flasks hence allowing 24 samples per experiment. We have customized the slide flasks by drilling a 3 mm width hole at the center of the slide flasks and then glued 12 mm glass coverslips for immunostaining and live imaging experiments. For electron microscopy and patch-clamp experiments, we have generated three-tier slide flasks by drilling 3 mm width hole at the center of the slide flask and then glueing the 12 mm Aclar-foil over the 16 mm glass coverslip. The 2D-clinostat was installed in an incubator and cells were cultured and exposed to SMG at 37°C and 5% CO_2 whereas the control CMs were cultured in slide-customized flasks and were kept in the incubator but not placed on the 2D clinostat. In the Slide-flask 2D-clinostat, the fast and constant rotation at 60 rpm induces gravity vector randomization and during this rotation, to avoid any fluid movements inside the flasks, it is necessary to remove all the air bubbles. Rotation of flask generates acceleration, which exposes cells to SMG in the range from 0.012 *g* (at the 3 mm area from the center of rotation) to 0.036 *g* at the farther distance (Eiermann et al., 2013). For all the studies, the cells from the central 3 mm area, which were exposed to microgravity of 0.012 *g* for different times and were harvested for further experiments.

MTT assay

The IMR90-CMs and iCell-CMs were seeded in a single channel ibidi slide and incubated in the cell culture incubator for 4 days. The cells were then exposed to SMG on 2D-Clinostat. Post 24 h, 48 and 72 h of exposure, 200 μL MTT solution was added and cells were incubated in the dark for 150 min. Then the medium was removed and formazan crystals formed in the cells were dissolved using 200 μL of DMSO followed by transfer into a 96 well plate. The absorbance was read at 570 nm using Softmax Pro M5e 96-well plate reader (Molecular Devices, Sunnyvale, CA, USA) (n = 9; three independent experiments) and represented as per cent cell death compared to that of control cells.

RNA isolation from CMs

RNA isolation was done by using RNAqueous™ Micro Total RNA Isolation Kit AM1931 from (Ambion). Total RNA concentration was measured by UV-Vis spectrophotometer nanodrop2000c (Thermo Fisher Scientific). Furthermore, samples were measured on the Fragment Analyzer 5200 (Agilent). In case of gDNA

contamination, the DNase I (Thermo Fisher Scientific) digest was performed. Then samples were processed for library preparation for RNA seq.

RNAseq library preparation

Sequencing-ready libraries were produced using a QuantSeq 3′ mRNA-Seq Library Prep Kit FWD for Illumina (015UG009V0241) following the standard procedures, as described by Lexogen. Indexed library preparation was performed to allow multiplexed sequencing. 250 ng mRNA samples were used as input for the library preparation. Finished libraries were quality controlled on a Bioanalyzer device (Agilent), using the HS-DNA assay. The concentration of obtained libraries was quantified using a Qubit dsDNA HS assay (Thermo Fisher). A sequencing-ready pool of indexed libraries was prepared according to these quantifications.

Sequencing of prepared library

Samples were pooled in equimolar ratio and the library pool was quantified using a Qubit dsDNA HS assay kit (Thermo Fisher Scientific). Sequencing was performed on Illumina NextSeq 500 with a SR75 High Output by following Lexogen standard protocol. The transcriptome RNA-seq data were validated by qRT-PCR analysis of upregulated (Figure S7A) and downregulated genes (Figure S7B) (for prime sequence see Table S8).

SILAC iabelling and mass spectroscopy

We performed quantitative proteomics applying the "stable isotope labeling by/with amino acids in cell culture"(SILAC) methodology as described previously (Chen et al., 2015) to identify proteins dysregulated in under microgravity conditions in CMs. For this aim, hiPSCs were cultured with normal RPMI 1640 containing "heavy" and "light" arginine and lysine isotopes of both amino acids and supplemented with GlutaMAX (1%, v/v). The "heavy" SILAC RPMI medium (500 mL) was supplemented with 50 mg of 1-Arg-10 = L-[13C615N4] Arg. HCl, 25 mg of 2-Lys-8 = l-[13C615N2]Lys.HCl, 100 mg proline and 5 mL pen-strep. The composition of the "light" SILAC RPMI 1640 medium (500 mL) was similar but the heavy amino acids were replaced with 50 mg light 1-Arg-0 = l-[12C614N4]Arg.HCl and 25 mg light 2-Lys-0 = l-[12C614N2] Lys.HCl) and 100 mg proline and 5 mL pen-strep. The hiPSCs were cultured in parallel in "heavy" and "light" SILAC media till the cells reached a confluence of more than 90% (day 0). Then cells were differentiated in SILAC media in the absence and presence of CHIR99021 (10 μM) and IWP-2 (5 μM) and 4 mM L-lactate as described by the differentiation protocol. In total after 20 days of differentiation, the "heavy" and "light" labelled CMs were further cultured in a maturation medium containing the "heavy" or the "light" amino acids at the same concentrations as shown above. The SILAC labelled experiments were divided into two groups; the "heavy" and the "light" isotope group. The "light" isotope labelled cells were exposed to SMG and the "heavy" isotope labelled cells were kept as ground control. After exposing the cells to SMG, CMs cells from both groups were lysed using standard RIPA lysis buffer (Sigma). Then "heavy" and "light" samples were mixed at a ratio of 1:1 and subjected to single-pot, solid-phase-enhanced sample-preparation (SP3) digestion following mass spectrometry analysis. All samples were analysed on a Q-Exactive Plus (Thermo Scientific) mass spectrometer that was coupled to an EASY nLC 1000 UPLC (Thermo Scientific) chromatograph. Peptides were loaded with solvent A (0.1% formic acid in water) onto an in-house packed analytical column (50 cm × 75 μm I.D., filled with 2.7 μm Poroshell EC120 C18, Agilent) and chromatographically separated at a constant flow rate of 250 nL/min using 60 or 150 min gradient of 5-30% solvent B (0.1% formic acid in 80% acetonitrile). The mass spectrometer was operated in data-dependent acquisition mode. The MS1 survey scan was acquired from 300-1750 m/z at a resolution of 70,000. The top 10 most abundant peptides were isolated within a 2 Da window and subjected to HCD fragmentation at a normalized collision energy of 27%. Precursors were dynamically excluded for 20 s. For bioinformatics data analysis all raw data from mass spectrometry were processed with Maxquant (version 1.5.3.8) using default parameters (Tyanova et al., 2016). Protein SILAC ratios were log2 transformed and normalized to the median. For every time point, a one-sample t-test was performed. Proteins with a p value < 0.05 and log2 change < -1 or >1 were considered significantly changing and subjected to profile clustering, which was generated using the z-scored mean values per group. A two-sample t-test was used to determine significantly enriched proteins. Potential contaminants were annotated based on the Crapome repository (Mellacheruvu et al., 2013).

Quantitative real-time PCR for gene expression analysis

The mRNA expression analysis was executed as we described previously (Nemade et al., 2020). In brief, 500 ng of mRNA was used to synthesize cDNA (high-capacity cDNA Synthesis Kit, qScript and Applied

bio-system). Then cDNA synthesis was diluted with highly pure RNAse free water at 1:5 ratio and then 2 μL of the diluted cDNA was used for qRT-PCR (Applied Biosystems 7500 FAST Real-Time PCR System) with the appropriate primers. GAPDH mRNA was used as an internal control.

Native whole-genome chromosome conformation capture (iHi-C 2.0) and data analysis

The effect of microgravity on the chromosome architecture in the CMs was investigated by the iHi-C 2.0 method as we described previously (Mizi et al., 2020). Briefly, CMs (0.3×10^6) were seeded on fibronectin-coated 12 cm^2 slide-flask and exposed to SMG for 48 h. Control CMs grown at *1 g* were used as control. After SMG exposure cells were gently removed from the slide and processed for iHi-C2.0. First, the nuclei were isolated for digestion and ligation in naïve condition, followed by purification and linearization for DNA library preparations. We initiated the library preparation by adding 10 bp unique molecular identifier (UMI) oligo provided with the Select High Sensitivity kit (Agilent). Then we performed the paired-end sequencing, adapter primer was used into the barcode library, while utilizing the TruSeq SR cluster kit (Illumina). As next step we used KAPA HiFi Hot start polymerase (KAPA Biosystems) to amplify the iHiC-2.0 library in 15 μL reaction. Then we subjected those purified libraries for NGS. The instrument used for NGS sequence read was HiSeq4000 (or equivalent capacity) platform (Illumina). It reads up to 15×10^7 read pairs each and each read length was 75 nt. Raw sequencing reads in each pair (.fastq files) were mapped independently to the human reference genome (hg19) using BWA-MEM after trimming of 5 nt from each end to eliminate identical *Nla*III sequence motifs. PCR duplicates were defined as those read pairs mapping to the same locations in the genome and carrying the same UMI, and were manually removed. Following this, reads were further filtered to remove any that did not precisely map next to genomic *Nla*II recognition sites. Similarly, read pairs with both ends mapping to the same *Nla*III fragment or with "dangling" ends were also removed. The resulting data matrcies were processed using "Bloom" for imputation to counter sparsity (Gusmao et al., 2020). Ultimately, the library of filtered mapped read pairs were normalized and converted to.hic files and visualized via Juicebox (Durand et al., 2016) to give rise to KR-normalised (Knight and Ruiz, 2012), interactive, and zoomable iHi-C maps. Compartment analysis was performed using the first principal component of the Hi-C matrices as described (Rao et al., 2017) and TAD boundaries were identified using default setting in (Kruse et al., 2016). Binarization and matrix subtractions were performed as previously described (Zirkel et al., 2018).

ATP assay

Intracellular ATP levels in CMs were determined using the ATPlite Luminescence Assay System (PerkinElmer, Waltham, MA) according to the manufacturer's instructions and the light intensity at 560 nm was quantified using the Softmax Pro M5e 96-well plate reader (Molecular Devices, Sunnyvale, CA, USA). The raw intensity data were normalized and presented as per cent changes of the ATP levels. Three independent experiments were performed in triplicates (n = 9).

Immunostaining (ICC)

CMs sarcomere assembly was detected by immunostaining of the cardiac-specific proteins ACTN2 and cardiac troponin T (cTnT). Cardiomyocytes were fixed by using ice-cold 99% methanol. Then cells were permeabilized with 0.3% TritonX-100 in the presence of 5% BSA. Then cells were washed and incubated with 1:200 diluted primary antibodies against α-actinin and cTnT at 37°C for 1 h. After 3 times washing with PBST, staining of the proteins was performed by incubating the cells for 1 h at RT with a secondary species-specific Alexa Fluor-488/568-conjugated secondary antibody (1:2000 dilution; Invitrogen, Darmstadt, Germany). The cells were washed and mounted on a slide with Prolong Gold anti-fade mount with DAPI (Invitrogen, Darmstadt, Germany). Fluorescence microscopy was performed with the Axiovert 200 fluorescence microscope and images were then analyzed using Axiovision 4.3 software (Carl Zeiss).

Measurement of intracellular ROS in CMs post SMG exposure

The intracellular ROS production in CMs was determined by dihydroethidium (DHE) staining as described previously (Nemade et al., 2018). Briefly, cell staining was performed by culturing the cells with 5 μM DHE for 30 min at 37°C and 5% CO_2. Then cells were washed with DPBS (Ca^{2+} and Mg^{2+} free PBS; Thermo Fisher Scientific) and fixed with Prolong® Gold anti-fade mount with DAPI (Invitrogen, Darmstadt, Germany). Fluorescence microscopy was performed with the Axiovert 200 fluorescence microscope and fluorescence was quantified using Axiovision 4.3 software (Carl Zeiss). The method is based on the oxidation of DHE by ROS to form ethidium bromide, which penetrates the nucleus and bind to DNA and due to red

punctate patterns appearing inside the nucleus. Analysis of arbitrary images has been executed by image J as described previously (Huang et al., 2019). Five images of c-CMs (in total n = 71 cells) and SMG-CMs (in total n = 53 cells) from three independent experiments (3 slides) were selected and all the cells in each image were counted for positive and negative red nuclear staining. Then the percent positive staining was calculated and represented in the graph as % DHE staining. Additionally, we determined the intracellular level of ROS, by using the 20, 70 dichlorofluorescin diacetate (DCFH-DA) test according to the manufacturer's instructions (ABIN2344999, Cell Biolabs, San Diego, CA, USA). After 48 h of SMG, the cells were washed with PBS and incubated with DCFH-DA (10 μM) for 30 min at 37°C. DCFH-DA diffuses into cells and is deacetylated by cellular esterase to non-fluorescent DCFH, which is rapidly oxidized to highly fluorescent DCF in presence of ROS. The fluorescence intensity was measured using Softmax Pro M5e 96-well plate reader (Molecular Devices, Sunnyvale, CA, USA) with excitation and emission wavelengths of 485 and 535 nm, respectively (n = 9, three independent experiments, performed in triplicates). All the fluorescence intensities are normalized with control cells (100%) and represented as a percentage of the control.

Determination of the NO-derived-reactive nitrogen species (RNS)

The NO-derived RNS were quantified with the OxiSelect™ Intracellular Nitric Oxide Assay Kit following the manufacturer's instructions (Cell Biolabs, Inc., San Diego, CA) (Novo and Parola, 2008). Experiments were performed in three independent experiments, performed in triplicates (n = 9). Fluorescence was quantified in a fluorometric plate reader at 480 nm/530 nm (expressed as percent of the absolute values of RNS in c-CMs.

Transmission Electron Microscopy of CMs

The TEM experiments were performed as we described previously (Nemade et al., 2018). Briefly, 48 h SMG exposed CMs and control CMs, were seeded into specially designed slide flask having 3 tier detachable ACLAR® embedding films (Ted Pella, Inc. USA) which were glued to slide flask shown in (Figure S1). The ultrathin slides (~70 nm) were prepared by using Leica EM UC6 Ultramicrotome (Leica, Germany). Then slices were subjected to dual stain with uranyl acetate followed by lead citrate. TEM imaging analysis was performed using a transmission electron microscope (EM109, Zeiss, Germany) equipped with a frame-transfer-CCD camera. Using ImageJ, the mitochondrial length was determined and plotted in a box plot.

Calcium imaging of CMs post SMG exposure

CMs (0.3×10^6) were seeded on fibronectin-coated 12 cm^2 slide-flasks and were exposed to SMG for 48 h. Cells were then loaded with 2 μM FLUO-4 AM (Invitrogen) for 30 min at 37°C and 5% CO_2, and thereafter were washed with basal media. Local [Ca^{2+}] oscillations were then recorded by applying the line scan mode of the Olympus FV1000 microscope using a 60× oil immersion objective and an excitation wavelength of 488 nm, as described previously (Walter et al., 2016). Upon capturing, background-correction was applied to all transients For both SMG and c-CMs, we recorded seventy independent readings to perform a robust statistical analysis (n = 70, from 2 independent cell preparations).

β-galactosidase staining

To detect the activation of β-Galactosidase as a parameter for senescence processes in CMs the β-Galactosidase activity Cell Event™ Senescence Green Detection Kit (Thermo Fisher Scientific). The staining was performed at 37°C in the absence of CO_2 for 1 to 2 h. The enzyme cleavage the substrate β-galactosidase into monosaccharides in an acidic pH medium. A fluorescence product covalently interacts with intracellular proteins. Quantification of the fluorescence intensity was performed at absorption 490 nm and emission wavelength of 514 nm (three independent experiments, n = 35 CMs from each condition) was determined by the imageJ software. Then the captured images were evaluated by imageJ to analyse the senescence versus non-senescent CMs. CMs from each condition (c-CMs and SMG-CMs) were selected and the GFP intensity was quantified using the imageJ software. Then the raw intensity data were plotted.

Mitochondrial membrane potential (mΔψ) assay

Mitochondrial membrane potential differences in CMs were determined by using JC-1 dye staining. The CMs (0.3×10^6) were seeded onto fibronectin-coated 12 cm^2 slide-flask. After 72 h incubation, the cells

were exposed to SMG for the next 48 h by keeping respective ground control cells. Then cells were loaded with 10 μM JC-1 dye (AAT Bioquest, CA) and incubated for 30 min at 37°C, 5% CO_2. After incubation, the cells were washed two times with DPBS. H_2O_2 (100 nM; 48 h) was used as a positive control. After washing, cells were cultured in normal media and then the cells were subjected to microscopy.

Protein expression analysis of SMG exposed CMs by Western blot

The SMG exposed and in parallel, the ground control cells from the central 3 mm area of the flask were scratched and transferred into a 15 mL tube with 5 mL ice-cold PBS. After centrifugation at 1500 rpm for 5 min protein was extracted by bath sonication using RIPA lysis buffer (50 mM Tris-HCl pH 7.6, 150 mM NaCl, 1% TritonX-100, 1% sodium deoxycholate, 0.1% SDS; Sigma). Isolated protein was then quantified by using a standard BCA reagent kit (Thermo Fisher Scientific). Then protein samples were separated by 20% SDS-polyacrylamide gel electrophoresis. After electrophoresis proteins were transferred into the nitrocellulose membrane by using blot, a dry blot instrument (Thermo Fisher Scientific) and the transfer buffer. After the transfer, membranes were treated with 5% non-fat milk in TBS buffer for 1 h at room temperature. Membranes were then treated overnight with the primary antibodies in a dilution of 1:200 to label the targeted protein. Membranes were then washed 3 times with TBST. The dyes IRDye 680CW and 800CW (Thermo Fisher Scientific) were used. Membranes were then incubated with the secondary antibody (1:12000 dilution) for 1 h. Then membranes were washed again for 3 times and then protein bands were detected by using the Odyssey Infrared Imaging System (LI-COR).

Whole-cell patch-clamp of CMs post SMG exposure

Electrophysiological recordings were performed using the whole-cell configuration of the patch-clamp technique as described previously (Hamill et al., 1981). Patch pipettes were prepared from thick-walled borosilicate glass capillaries (1.5/0.84 mm OD/ID; World Precision Instruments) using a P97 Micropipette puller (Sutter Instruments) and had resistances between 5 and 7 MΩ when filled with the Cs-based internal solution. The bath was connected to ground via 120 mM sodium chloride agar bridges. Currents were acquired at 50 kHz and filtered at 10 kHz using an EPC9 amplifier (HEKA, Germany) controlled with HEKAs Pulse software. Leak and capacitive currents were subtracted online by use of a –P/5 protocol and series resistance was compensated electronically by up to 80%. All experiments were performed at room temperature and from a holding potential of −80 mV. During the recordings, cells (n = 8 for c-CMs and n = 6 for SMG-CMs) were continuously superfused with external solution containing (in mM) 120 NaCl, 5 KCl, 3.6 $CaCl_2$, 1 $MgCl_2$, 10 HEPES, 20 tetraethylammonium chloride and 2 4-aminopyridine, with the pH adjusted to 7.4 using NaOH. The pipette solution contained (in mM) 120 CsCl, 3 $MgCl_2$, 10 ethylene glycol-bis(2-aminoethylether)-N,N,N′,N′-tetraacetic acid (EGTA), 5 HEPES and 4 MgATP, with the pH adjusted to 7.3 using CsOH. Ca^{2+} currents were recorded in response to 100 ms voltage-steps after a pre-pulse at −40 mV to inactivate Na^+ channels and normalized by the whole-cell capacitance to give current density values. To construct current-voltage-relationships, peak current densities measured between −50 and 60 mV (10 mV increments) were plotted as a function of the test potential and fitted with a combined Ohm-Boltzmann equation.

Real-time imaging of mitochondrial ROS by MitoTimer

To monitor the mitochondrial ROS a transgenic hiPSCs line (IMR90) was generated allowing the expression of the genetically encoded sensor protein MitoTimer in a Tet-inducible manner. MitoTimer is coding for DyRed1-E5 protein (a mutant form of DsRed protein) which is sensitive to free radicals. It changes its fluorescence colour from green to red in response to an increased ROS level and high mitochondrial turnover (Hernandez et al., 2013; Laker et al., 2014). Generation of the hiPSC line was performed using the Gateway® Cloning system to generate the donor vector with MitoTimer integrated between the 5′ and -3′ terminal repeats. As a second step, the *piggyBac* transposon system was used to drive the genomic integration of MitoTimer in chromosomal DNA for stable expression (see Figure S2).

Generation of ACTN2-eGFP$^+$ hiPSC line

To monitor CM sarcomere contraction and relaxation in real-time we generated a α−cardiac actinin (ACTN2)-enhanced green fluorescent protein (eGFP$^+$)-hiPSC line by the CRISPR-Cas9 (Sachinidis, 2021) and the homology-directed recombination (HDR) approach as we described more recently (Acharya et al., 2022). A brief description is indicated in Figure S3. The contractile velocity of c-CMs and SMG-CMs was determined by analysing the videos using the VA1.9 software (Acharya et al., 2022).

QUANTIFICATION AND STATISTICAL ANALYSIS

For all experiments, the statistical data are represented as mean ± standard deviation (SD). To calculate the p value of significance, a two-tailed Student's test (t-test) from Microsoft Excel software was used and p values <0.05 were considered as statistically significant. The RNAseq data were analysed by the one-way ANOVA followed by Tukey post hoc tests for statistics using the RStudio (https://www.rstudio.com/products/rstudio/).